Spin-Induced Polarizations and Non-Reciprocal Directional Dichroism of the Room-Temperature Multiferroic $BiFeO_3$*

Randy S. Fishman[1], Jun Hee Lee[1], Sándor Bordács[2], István Kézsmárki[2], Urmas Nagel[3], and Toomas Rõõm[3]
[1] *Materials Science and Technology Division, Oak Ridge National Laboratory, Oak Ridge, Tennessee 37831, USA*
[2] *Department of Physics, Budapest University of Technology and Economics and MTA-BME Lendület Magneto-optical Spectroscopy Research Group, 1111 Budapest, Hungary and*
[3] *National Institute of Chemical Physics and Biophysics, Akademia tee 23, 12618 Tallinn, Estonia*
(Dated: August 26, 2015)

A microscopic model for the room-temperature multiferroic $BiFeO_3$ that includes two Dzyaloshinskii-Moriya interactions and single-ion anisotropy along the ferroelectric polarization predicts both the zero-field spectroscopic modes as well as their splitting and evolution in a magnetic field. Due to simultaneously broken time-reversal and spatial-inversion symmetries, the absorption of light changes as the magnetic field or the direction of light propagation is reversed. We discuss three physical mechanisms that may contribute to this absorption asymmetry known as non-reciprocal directional dichroism: the spin current, magnetostriction, and single-ion anisotropy. We conclude that the non-reciprocal directional dichroism in $BiFeO_3$ is dominated by the spin-current polarization and is insensitive to the magnetostriction and easy-axis anisotropy. With three independent spin-current parameters, our model accurately describes the non-reciprocal directional dichroism observed for magnetic field along $[1,-1,0]$. Since some modes are almost transparent to light traveling in one direction but opaque for light traveling in the opposite direction, $BiFeO_3$ can be used as a room-temperature optical diode at certain frequencies in the GHz to THz range. Our work demonstrates that an analysis of the non-reciprocal directional dichroism spectra based on an effective spin model supplemented by first-principles calculations can produce a quantitative microscopic theory of the magnetoelectric couplings in multiferroic materials.

PACS numbers: 75.25.-j, 75.30.Ds, 75.50.Ee, 78.30.-j

I. INTRODUCTION

$BiFeO_3$ is the only material known to exhibit multiferroic behavior at room temperature. Because its ferroelectric (FE) transition temperature[1] $T_c \approx 1100$ K is significantly higher than its Néel transition temperature[2] $T_N \approx 640$ K, $BiFeO_3$ is a type I multiferroic. Although the non-magnetic FE polarization[3] $P^{FE} \approx 90\,\mu C/cm^2$ is much larger than the magnetic contribution[4–7] induced by the distorted spin cycloid[2,8–11], the magnetic domain distribution of $BiFeO_3$ can be manipulated by an applied electric field[8,12].

A great deal has been learned about $BiFeO_3$ since the first single crystals became available for inelastic neutron scattering[13–15], Raman scattering[16,17], and THz spectroscopy[18,19] measurements. It is now understood that two sets of interactions control the cycloid of $BiFeO_3$: two Dzyaloshinskii-Moriya (DM) interactions produced by broken inversion symmetry and a single-ion anisotropy[20] (ANI) K along the direction of the FE polarization $\mathbf{P}^{FE}$. Whereas the DM interaction[2] D_1 perpendicular to $\mathbf{P}^{FE}$ is responsible for the long 62 nm cycloidal period, the DM interaction[4,21–23] D_2 along $\mathbf{P}^{FE}$ is responsible for a small cycloidal tilt[21]. Above the critical magnetic field H_c, the cycloidal tilt develops into the weak ferromagnetic (FM) moment[5,6,24] of a G-type antiferromagnet (AF) that is isosymmetrically canted by an antiferrodistortive rotation ($R_4^+[1,1,1]$) of the $R3c$ structure[23].

Inelastic neutron scattering measurements[13–15] were used to extract the AF nearest- and next-nearest neighbor exchange interactions[25] $J_1 = -5.32$ meV and $J_2 = -0.24$ meV between the $S = 5/2$ Fe^{3+} spins on the pseudo-cubic unit cell sketched in Fig.1(a) with lattice constant $a = 3.96\mathring{A}$. However, those measurements lacked the sensitivity to resolve the ordering wavevectors on either side of the G-type AF wavevector $\mathbf{Q}_0 = (2\pi/a)[0.5, 0.5, 0.5]$ at $(2\pi/a)[0.5 \pm \delta, 0.5, 0.5 \mp \delta]$, where $\delta \approx 0.0045$ is inversely proportional to the cycloidal period $a/(\sqrt{2}\delta)$. Recent neutron scattering measurements[26] with higher precision were able to distinguish the two cycloidal ordering wavevectors and found that[25] $D_1 = 0.18$ meV and $K = 0.0039$ meV. But even those measurements lacked the precision to obtain D_2, which was set to zero.

By contrast, the frequencies of the spin-wave (SW) modes at the ordering wavevector $\mathbf{Q}$ can be precisely measured with Raman scattering[16] and THz spectroscopy[18,19]. The parameters K, D_1, and D_2 were

*Copyright notice: This manuscript has been authored by UT-Battelle, LLC under Contract No. DE-AC05-00OR22725 with the U.S. Department of Energy. The United States Government retains and the publisher, by accepting the article for publication, acknowledges that the United States Government retains a non-exclusive, paid-up, irrevocable, world-wide license to publish or reproduce the published form of this manuscript, or allow others to do so, for United States Government purposes. The Department of Energy will provide public access to these results of federally sponsored research in accordance with the DOE Public Access Plan (http://energy.gov/downloads/doe-public-access-plan).

estimated by fitting the frequencies[27] of the four observed zero-field THz modes. With no remaining adjustable parameters, that same model predicted[28] the evolution and activation of the THz modes[19] in a magnetic field along $[0, 0, 1]$.

We now use this microscopic model to predict the asymmetry $\Delta\alpha(\omega)$ in the absorption $\alpha(\omega)$ of light when the direction of the magnetic field or, equivalently, the direction of light propagation is reversed. Called non-reciprocal directional dichroism (NDD), absorption asymmetry was first observed by Hopfield and Thomas[29] over 50 years ago in CdS. Much more recently, the precise symmetry requirements for NDD in magnetic materials were systematically investigated by Szaller *et al.* [30]. Strong NDD is expected for the spin excitations of multiferroic materials when both time reversal and spatial inversion symmetries are broken by the spin state. Both the magnetic and electric components of THz radiation can excite SWs in multiferroic materials. The NDD exhibited by simultaneously electric- and magnetic-dipole active excitations has been extensively studied in $Ba_2CoGe_2O_7$ [31–34], $Sr_2CoSi_2O_7$ [34], $Ca_2CoSi_2O_7$ [34], $Gd_{0.5}Tb_{0.5}MnO_3$ [35], and $Eu_{0.55}Y_{0.45}MnO_3$ [36].

Because the cycloidal spin state is produced by the competition between DM, exchange, and ANI interactions, three distinct physical mechanisms can produce NDD in $BiFeO_3$: the spin current (SC) driven by the DM interactions, magnetostriction (MS) or the electric-field induced changes in the exchange interactions, and the electric-field induced changes in the ANI. Remarkably, the dynamical magnetoelectric coupling governing the NDD in $BiFeO_3$ is dominated by the two sets of SC polarizations associated with D_1 and D_2. Qualitatively, the SC dominates the magnetoelectric coupling in $BiFeO_3$ because spin fluctuations $\delta\mathbf{S}_i$ are transverse to the almost collinear, cycloidal spin state $\langle\mathbf{S}_i\rangle$. Since $\delta\mathbf{S}_i \times \langle\mathbf{S}_j\rangle \neq 0$ but $\delta\mathbf{S}_i \cdot \langle\mathbf{S}_j\rangle \approx 0$ (for nearby sites i and j) and the ANI is extremely weak, spin fluctuations more strongly affect the SC-induced polarization than the MS- and ANI-induced polarizations.

As a fraction of the total light absorption at a given wavelength, NDD is most pronounced for a mode with fluctuations out of the cycloidal plane at 15.5 cm^{-1}. At this wavenumber, $BiFeO_3$ is almost transparent for light traveling in one direction but opaque for light traveling in the opposite direction. Therefore, $BiFeO_3$ can be used as an optical diode that operates up to room temperature.

Despite the success of our model describing the NDD for magnetic field along $[1, -1, 0]$, several questions remain open. Although our model predicts NDD to be absent for light propagating along $\mathbf{k} = [0, 0, 1]$, a static magnetic field along $[\eta, \eta, \kappa]$, and THz electric-field orientation $\mathbf{e} = [1, 1, 0]$ or $[1, -1, 0]$, weak NDD has been observed for a magnetic field along $[1, 1, 0]$ under those conditions. An optical misalignment of the THz electric- and magnetic-field vectors $\mathbf{e}$ and $\mathbf{h} = \mathbf{k} \times \mathbf{e}$ may be responsible for this effect. In addition, the mean absorption $\bar{\alpha}(\omega)$ (the absorption $\alpha(\omega)$ averaged over positive and negative magnetic fields) is not as accurately predicted by our model as the NDD.

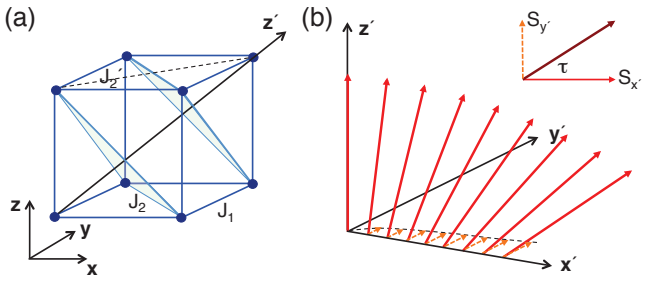

FIG. 1: (Color online) (a) The exchange interactions J_1 and J_2 on the pseudo-cubic lattice for $BiFeO_3$ with Fe^{3+} ions at the corners of the cube and two hexagonal layers shown. Due to the rhombohedral distortion along $\mathbf{z}'$, J_2' and J_2 may be slightly different. (b) The spin state in zero magnetic field, both with electric polarization along $\mathbf{z}'$. The canting of the spins out of the $\{x', z'\}$ plane is indicated by the angle τ in the inset. The variation of the canted component along x' is also shown by the dashed line in (b).

This paper complements a recent work[37] that presents detailed experimental results for both the individual absorptions and the NDD. We have divided this paper into six sections. Section II presents our microscopic model and Section III presents the predicted mode frequencies. Section IV describes the three polarization mechanisms and presents results for the magnetization and polarization matrix elements, with symmetry relations provided by Local Spin-Density Approximation (LSDA)+U calculations. Results for the NDD are presented in Section V. Section VI contains a discussion and conclusion. While Appendix A summarizes the experimental details, Appendices B, C, and D treat the SC-, MS-, and ANI-induced polarizations, respectively. Appendix E provides the THz absorption parameters. Appendix F summarizes the first-principles calculations used to help construct the polarization operators. For convenience, the unit vectors used in this paper are given in Table I.

II. MICROSCOPIC MODEL

In a magnetic field $\mathbf{H} = H\mathbf{m}$, the spin state and SW excitations of $BiFeO_3$ are evaluated from the microscopic Hamiltonian

$$\begin{aligned}\mathcal{H} = &-J_1 \sum_{\langle i,j\rangle} \mathbf{S}_i \cdot \mathbf{S}_j - J_2 \sum_{\langle i,j\rangle'} \mathbf{S}_i \cdot \mathbf{S}_j \\ &+D_1 \sum_{\langle i,j\rangle} (\mathbf{z}' \times \mathbf{e}_{i,j}/a) \cdot (\mathbf{S}_i \times \mathbf{S}_j) \\ &+D_2 \sum_{\langle i,j\rangle} (-1)^{n_i}\, \mathbf{z}' \cdot (\mathbf{S}_i \times \mathbf{S}_j) \\ &-K \sum_i (\mathbf{z}' \cdot \mathbf{S}_i)^2 - 2\mu_B H \sum_i \mathbf{m} \cdot \mathbf{S}_i, \end{aligned} \tag{1}$$

TABLE I: **Unit vectors**

$\mathbf{x}$, $\mathbf{y}$, $\mathbf{z}$	Pseudo-cubic laboratory reference frame
$\mathbf{z}' = \mathbf{z}'_m$	Orientation of the electric polarization $\mathbf{P}^{\rm FE}$ along one of the cubic diagonals
$\mathbf{x}'$, $\mathbf{y}'$, $\mathbf{z}'$	Cycloidal reference frame
$\mathbf{x}'_m$, $\mathbf{y}'_m$, $\mathbf{z}'_m$	Cycloidal reference frame for domain m
$\mathbf{u}$	$\mathbf{x}$, $\mathbf{y}$, or $\mathbf{z}$
$\mathbf{m}$	Orientation of the static magnetic field
$\mathbf{n}_i$	Local single-ion ANI axis
$\mathbf{k}$	Direction of light propagation
$\mathbf{e}$	Orientation of the THz electric field
$\mathbf{h}$	Orientation of the THz magnetic field

where $\mathbf{e}_{i,j} = a\mathbf{x}$, $a\mathbf{y}$, or $a\mathbf{z}$ connects $\mathbf{R}_i$ with its nearest neighbor $\mathbf{R}_j = \mathbf{R}_i + \mathbf{e}_{i,j}$. Since the unit vector $\mathbf{z}'$ points along a cubic diagonal parallel to the FE polarization $\mathbf{P}^{\rm FE}$, the D_1 sum has the form proposed by Katsura *et al.*[38]. The hexagonal layers normal to $\mathbf{z}'$ are separated by $c = a/\sqrt{3}$ and are labeled by the integer $n_i = \mathbf{R}_i \cdot \mathbf{z}'/c$. Consequently, the D_2 sum alternates sign from one hexagonal layer to the next. Notice that the local DM interactions $D_1\,(\mathbf{z}' \times \mathbf{e}_{i,j}/a)$ and $D_2\,\mathbf{z}'$ are, respectively, perpendicular and parallel to $\mathbf{z}'$.

There are eight possible orientations for $\mathbf{P}^{\rm FE} \parallel \mathbf{z}'$ along the four cubic diagonals. For every possible $\mathbf{z}'$, the three magnetic domains have different $\mathbf{x}'$ and $\mathbf{y}'$. When $\mathbf{z}' = [1,1,1]$ (all unit vectors in Table I are assumed normalized to 1), the possible orientations for the x' axis are $\mathbf{x}'_1 = [1,-1,0]$, $\mathbf{x}'_2 = [1,0,-1]$, and $\mathbf{x}'_3 = [0,1,-1]$ with corresponding $\mathbf{y}'_m = \mathbf{z}' \times \mathbf{x}'_m$. These three magnetic domains have cycloidal ordering wavevectors

$$\mathbf{Q}_m = \mathbf{Q}_0 + \frac{2\sqrt{2}\pi\delta}{a}\mathbf{x}'_m. \tag{2}$$

Hence, the ordering wavevectors for different domains are $\mathbf{Q}_1 = (2\pi/a)[0.5+\delta, 0.5-\delta, 0.5]$, $\mathbf{Q}_2 = (2\pi/a)[0.5+\delta, 0.5, 0.5-\delta]$, and $\mathbf{Q}_3 = (2\pi/a)[0.5, 0.5+\delta, 0.5-\delta]$. In terms of $\delta \ll 1$, the period of the cycloid in zero field is $a/(\sqrt{2}\delta) \approx 62$ nm.

As mentioned above, the DM interactions D_1 and D_2 only couple nearest-neighbor sites. In a previous formulation[27,28] of this microscopic model, D_1 coupled next-neighbor sites within the same hexagonal layer. Due to the very long cycloidal period $p \gg a$ of $BiFeO_3$, the equilibrium and dynamical properties of these two Hamiltonians are the same up to errors of order $\delta^2 \approx 2\times10^{-5}$. Specifically, earlier predictions for the SW mode frequencies[27,28] and critical magnetic field[39] are unchanged. However, the earlier DM interaction D_1 is now multiplied by $\sqrt{2}$. Because the nearest-neighbor DM interactions are much larger than those between next-neighbor spins, the Hamiltonian above provides a close connection with recent first-principles calculations[23,40].

Since the D_1 and D_2 terms in $\mathcal{H}$ depend only on $\mathbf{z}'$, $\mathcal{H}$ is independent of the magnetic domain. For a specific domain m, the first SC term can be written $V_1^{\rm SC} = \sqrt{2}D_1 N\,\mathbf{y}' \cdot \mathbf{T}_1$, where

$$\mathbf{T}_1 = \frac{1}{N}\sum_{\langle i,j\rangle^{\mathbf{x}}}\Big\{\mathbf{S}_i \times \mathbf{S}_j\Big\},\ \ m = 1,2, \tag{3}$$

$$\mathbf{T}_1 = \frac{1}{N}\sum_{\langle i,j\rangle^{\mathbf{y}}}\Big\{\mathbf{S}_i \times \mathbf{S}_j\Big\},\ \ m = 3, \tag{4}$$

where $\langle i,j\rangle^{\mathbf{u}}$ is a sum over nearest neighbors with $\mathbf{R}_j - \mathbf{R}_i = a\mathbf{u}$. These relations assume that the spins on each hexagonal layer depend only on the integer $r = \sqrt{2}\mathbf{x}' \cdot \mathbf{R}_i/a$. So for domain 2, $\mathbf{S}(\mathbf{R}_i + a\mathbf{x}) = \mathbf{S}(\mathbf{R}_i - a\mathbf{z})$. The cross products in Eqs.(3) and (4) couple spins with indices r and $r+1$ on neighboring layers.

The second SC term $V_2^{\rm SC}$ proportional to D_2 can be written $V_2^{\rm SC} = D_2 N\,\mathbf{z}' \cdot \mathbf{T}_2$, where

$$\mathbf{T}_2 = \frac{1}{N}\sum_{\langle i,j\rangle}(-1)^{n_i}\Big\{\mathbf{S}_i \times \mathbf{S}_j\Big\}. \tag{5}$$

Like $V_1^{\rm SC}$, $V_2^{\rm SC}$ also couples neighboring spins on neighboring layers.

The nearest- and next-nearest neighbor exchange interactions[25] $J_1 = -5.32$ meV and $J_2 = -0.24$ meV were obtained from recent inelastic neutron scattering measurements[13–15] between 5.5 meV and 72 meV. On the other hand, the small interactions D_1, D_2, and K that control the cycloid can be obtained from THz spectroscopy measurements[18,27] below 5.5 meV (44.3 cm^{-1}) in zero magnetic field.

We have neglected the broken spatial symmetry between the exchange interactions due to the rhombohedral distortion. While all J_1 interactions must remain the same due to the rotational C_3 symmetry about $\mathbf{z}'$, J_2 may reflect the rhombohedral distortion. For example, next-nearest neighbors separated by $\mathbf{R}_1 = a(\mathbf{x}+\mathbf{y})$ and $\mathbf{R}_2 = a(\mathbf{x}-\mathbf{y})$ may experience slightly different exchange interactions, denoted by J_2' and J_2 in Fig.1(a), because $\mathbf{R}_1 \cdot \mathbf{z}' = 2a/\sqrt{3}$ while $\mathbf{R}_2 \cdot \mathbf{z}' = 0$. However, based on the excellent agreement between theory and experiment for the mode frequencies reported in Section III and because J_2 is already so small, we expect this exchange anisotropy to have a very minor effect on the NDD.

For a given set of interaction parameters, the spin state of $BiFeO_3$ is obtained by minimizing the energy $E = \langle\mathcal{H}\rangle$ over a set of variational parameters[28]. Fixing $\delta = 1/q$, where $q \gg 1$ is an integer, the energy E is minimized over the variational parameters on a unit cell with q sites along $\mathbf{x}'$ and two hexagonal layers. The spin state on layer n is assumed to be identical to the spin state on layer $n+2$. The wavevector parameter δ is determined as a function of field by an additional minimization loop over q. In zero field, $\delta \approx 0.0045$ and $q = 222$. We verify that the corresponding spin state provides at least a metastable minimum of the energy E by checking that the classical forces on each spin vanish.

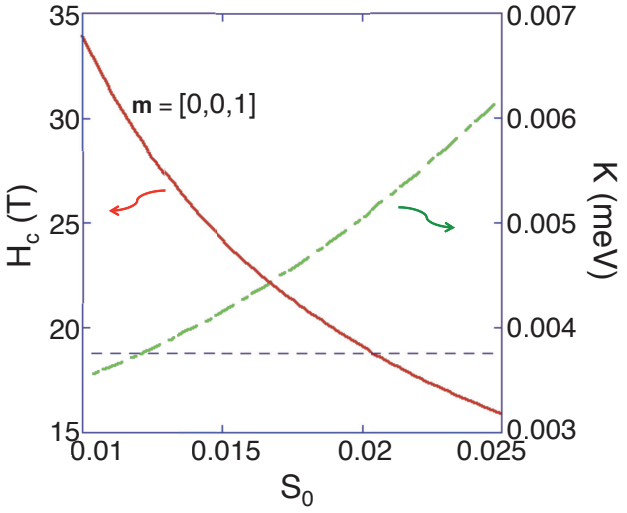

FIG. 2: (Color online) The predicted critical field (solid) versus S_0 for field orientation $\mathbf{m} = [0, 0, 1]$. The horizontal line is the experimental value[5] for H_c. Also plotted is the single-ion ANI K (dash-dot) versus S_0.

Ignoring the cycloidal harmonics $C_{l>1}$ produced by D_2 and K but including the tilt[21] τ produced by D_2, the spin state in zero field can be approximated by

$$S_{x'}(\mathbf{R}) = S(-1)^{n+1}\cos\tau\sin(2\pi\delta r), \quad (6)$$
$$S_{y'}(\mathbf{R}) = S\sin\tau\sin(2\pi\delta r), \quad (7)$$
$$S_{z'}(\mathbf{R}) = S(-1)^{n+1}\cos(2\pi\delta r). \quad (8)$$

This tilted cycloid is plotted in Fig.1(b). Averages over this state are readily performed using $\langle {S_{ix'}}^2\rangle = (S^2/2)\cos^2\tau$, $\langle {S_{iy'}}^2\rangle = (S^2/2)\sin^2\tau$, and $\langle {S_{iz'}}^2\rangle = S^2/2$. In zero field, averages over the tilted cycloid are fairly accurate because[27] even harmonics like C_2 vanish and $C_3 \approx 5\times10^{-3}$. Corrections to the averages are then of order ${C_3}^2 \approx 2.5\times10^{-5}$.

For comparison, the spin state of the canted AF at zero field can be simply written in terms of the canting angle τ within the $\{x', y', z'\}$ coordinate system as

$$\mathbf{S}_n = S[(-1)^{n+1}\cos\tau, \sin\tau, 0] \quad (9)$$

on hexagonal layer n. Recall that[27] $\sin\tau = S_0/S$ where $2\mu_B S_0$ is the weak FM moment of the AF phase along $\mathbf{y}'$ above H_c. Whereas susceptibility measurements[5] indicate that $S_0 = 0.015$, a recent neutron-scattering study[24] suggests that $S_0 \sim 0.05$ equivalent to $\tau \sim 1°$. By contrast, LSDA+U ($U = 5$ eV)[40] gives $S_0 = 0.014$, in agreement with the former experimental result. Note that $D_2 = -2J_1S_0/S = -2J_1\sin\tau$ is a linear function of S_0 and of $\sin\tau \approx \tau$.

We now adopt a different approach to estimate D_2. The three parameters D_1, D_2, and K are fixed by two conditions: the period of the cycloid must match the measured period and and the frequencies of the four predicted SW modes in zero field must match the measured frequencies[27]. A third condition is provided by the dependence of the predicted critical field H_c on S_0. As shown in Fig.2, the measured critical field of 18.8 T for $\mathbf{m} = [0, 0, 1]$ requires that[25] $S_0 = 0.02$, corresponding to $\tau = 0.008$ or 0.45°. While $D_1 \approx 0.180$ meV is virtually independent of S_0, D_2 linearly increases with S_0. Figure 2 indicates that K increases almost quadratically with S_0 from a value of $K = 0.0031$ meV when $S_0 = 0$. Corresponding to $S_0 = 0.02$, we obtain $D_2 = 0.085$ meV and $K = 0.0051$ meV. A somewhat smaller value $K = 0.0039$ meV was given in Ref.[26], which took $D_2 = 0$.

With other parameters fixed and $\mathbf{m} = [1, -1, 0]$, a value of D_2 smaller than about 0.079 meV would stabilize a different canted AF phase above H_c with spins tilted above and below the $\{x', y'\}$ plane due to the dominant single-ion ANI. Hence, the coplanar AF phase of Eq.(9) is barely stabilized by the second DM interaction.

III. SPECTROSCOPIC MODE FREQUENCIES

Using the parameters given above, $\mathcal{H}$ predicts the evolution of the modes with magnetic field[19,28,37] for all orientations $\mathbf{m}$. SW modes at the ordering wavevector $\mathbf{Q}$ can be labeled[41] as in-cycloidal-plane Φ_m modes and out-of-cycloidal-plane Ψ_m modes. In an extended zone scheme, those mode frequencies are plotted versus q/δ for wavevector $(2\pi/a)[0.5 + q, 0.5, 0.5 - q]$ in Fig.3(a). For simplicity, Φ_m and Ψ_m denote both the modes and their frequencies. Neglecting higher spin harmonics, $\Phi_m = |m|\Psi_0$ and $\Psi_m = \Psi_0\sqrt{1+m^2}$. It follows that $\Phi_1 = \Psi_0$.

Higher harmonics generated by the tilt and ANI split each mode with $m \geq 1$ into two labeled $\Phi_m^{(1,2)}$ or $\Psi_m^{(1,2)}$. For the predicted parameters of $BiFeO_3$, those modes are plotted versus wavevector in Fig.3(b). While the $m = 1$ modes are strongly affected by the spin harmonics, the former mode scheme remains fairly accurate for $m > 1$. Because the splitting of the low-frequency modes was not considered, recent Raman studies[16,17] misidentified the observed modes with some out-of-plane modes mistaken for in-plane modes and vice versa.

Despite the substantial splitting of $\Phi_1^{(1)}$ and $\Phi_1^{(2)}$, $\Phi_1^{(1)}$ is only slightly larger than Ψ_0. The nearly degenerate $\Phi_1^{(1)}$ and Ψ_0 modes cannot be separated by THz measurements[18,19] in zero field.

In Fig.4, the predicted and measured[42] mode frequencies are plotted versus field for orientations $\mathbf{m} = [0, 0, 1]$, $[1, 1, 0]$, and $[1, -1, 0]$. Experimental data was not available for the THz modes above H_c for the last two field orientations. The experimental results for $\mathbf{m} = [1, 1, 0]$ and $[1, -1, 0]$ are presented here for the first time with experimental details summarized in Appendix A. Because its frequency was too low, $\Phi_1^{(2)}$ was not detected when $\mathbf{m} = [1, 1, 0]$ and $[1, -1, 0]$. The predicted mode frequencies of the stable domain(s) are presented in the solid curves: domain 1 for $\mathbf{m} = [0, 0, 1]$ and $[1, 1, 0]$ and do-

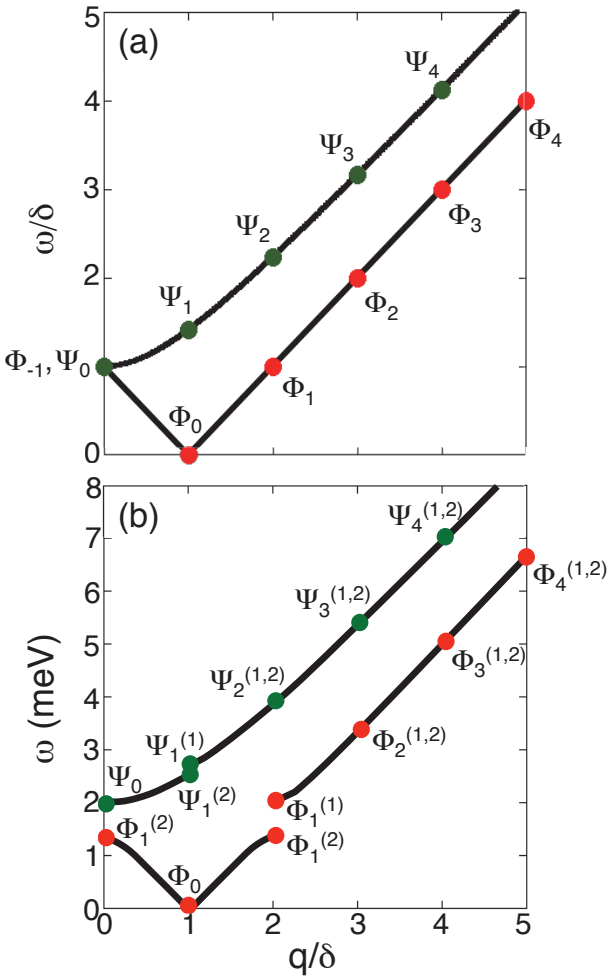

FIG. 3: (Color online) The mode spectra at multiples of the ordering wavevector in an extended zone scheme (a) without higher harmonics of the spin and (b) with higher harmonics for the predicted parameters of $BiFeO_3$.

mains 2 and 3 for $\mathbf{m} = [1, -1, 0]$. For $\mathbf{m} = [0, 0, 1]$, the mode that dips below $\Phi_1^{(2)}$ arises from metastable domains 2 and 3, as seen by the agreement with the dashed curve. Hence, metastable domains may survive up to about 10 T.

With $S_0 = 0.02$, the agreement between experiment and theory is even better than previously reported[19] for $\mathbf{m} = [0, 0, 1]$ with $S_0 = 0.015$. Nevertheless, that agreement deteriorates somewhat above 12 T, particularly for $\mathbf{m} = [1, -1, 0]$, when avoided mode crossings strongly affect the mode frequencies. It is possible that the trial spin state is not sophisticated enough at high magnetic fields. For example, the spin state in high magnetic fields may have a periodicity greater than two hexagonal layers.

Above H_c, the canted AF state of Eq.(9) supports only two modes that are labeled α and β in Fig.4. Because the transition at H_c is first order, the spectroscopic modes change discontinuously at the critical field.

The estimates given above for K, D_1, and D_2 were

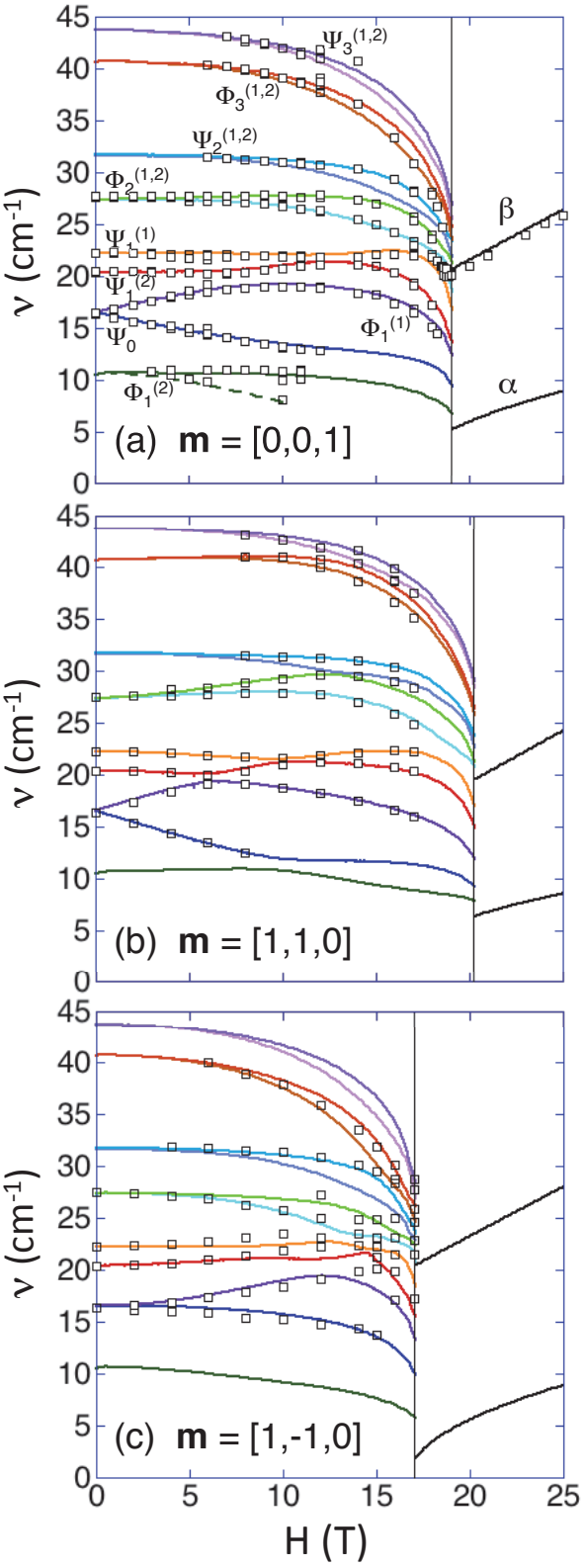

FIG. 4: (Color online) The theoretical mode spectra (solid curves) and experimental measurements (boxes) versus field for field orientations $\mathbf{m}$ = (a) $[0, 0, 1]$, (b) $[1, 1, 0]$, and (c) $[1, -1, 0]$. Solid vertical lines make the transition to the canted AF state. The dashed curve in (a) indicates the predicted $\Phi_1^{(2)}$ for metastable domains 2 and 3.

based on fits to the four THz modes observed[18,19] in zero field[43]. Experimental data points in Fig.4 indicate that those four modes correspond to $\Psi_0/\Phi_1^{(1)}$ (nearly degenerate), $\Psi_1^{(2)}$, $\Psi_1^{(1)}$, and $\Phi_2^{(1,2)}$ with frequencies 16.2, 20.7, 22.4, and 27.6 cm^{-1}, respectively.

IV. POLARIZATION MATRIX ELEMENTS

At zero magnetic field, only a few of the SW modes are optically active with finite magnetic-dipole resonance matrix elements $\langle n|\mathbf{M}|0\rangle$, where

$$\mathbf{M} = \frac{2\mu_{\rm B}}{N}\sum_i \mathbf{S}_i \tag{10}$$

is the magnetization operator, $|0\rangle$ is the ground state with no SWs, and $|n\rangle$ is the nth excited state with a single SW mode at the cycloidal wavevector $\mathbf{Q}$. At finite magnetic fields, all SW modes also have non-zero matrix elements $\langle n|\mathbf{P}^{\rm ind}|0\rangle$ of the induced electric polarization $\mathbf{P}^{\rm ind}$. The coexistence of the magnetic-dipole and polarization matrix elements is responsible for the NDD observed in the THz absorption spectra for field along $[1,-1,0]$. The physical mechanisms that contribute to $\mathbf{P}^{\rm ind}$ below $T_{\rm N}$ can be divided into three classes: SC, MS, and ANI.

For the SC- and MS-induced polarizations, we use LSDA+U calculations[40] to simplify the matrices connecting the induced polarizations with the spin operators. This greatly reduces the number of polarization parameters. In some instances, those matrices were simplified even further, either because some matrix elements were roughly equal or because additional matrix elements had a negligible effect on the NDD. Those additional simplifications are described in Ref.[40]. A summary of the first-principles calculations is provided in Appendix F.

This section expresses the induced polarizations in the cycloidal reference frame $\{x',y',z'\}$. In the laboratory reference frame $\{x,y,z\}$, the induced polarizations are given in Appendices B, C, and D.

A. SC-induced polarizations

The SC-induced polarization $\mathbf{P}^{\rm SC}$ is produced by shifts in the O locations due to the hopping of electrons between Fe $3d$ and O $2p$ orbitals[38,44,45]. The first SC-induced polarization is created by the well-known inverse DM interaction[38,46,47] corresponding to the D_1 term in the Hamiltonian. This polarization can be generally written as

$$P_{1\alpha}^{\rm SC} = \sum_\beta \lambda_{\alpha\beta}^{(1)} T_{1\beta}, \tag{11}$$

where $\mathbf{T}_1$ was defined by Eqs.(3) and (4). According to Eq.(B11), the four nonzero matrix elements of $\underline{\lambda}^{(1)}$ are $\lambda_{x'x'}^{(1)} = -\lambda_{y'y'}^{(1)} = \pm(c-d)$, $\lambda_{y'z'}^{(1)} = -2\sqrt{2}c$, and $\lambda_{z'y'}^{(1)} = -\sqrt{2}d$, where the plus sign is for domain 2 and the minus sign is for domains 1 or 3.

In a simplified version of the first SC-induced polarization with $c=d$, the diagonal terms $\lambda_{x'x'}^{(1)}$ and $\lambda_{y'y'}^{(1)}$ would vanish. Then $P_{1z'}^{\rm SC} = \lambda_{z'y'}^{(1)} T_{1y'}$ and $P_{1y'}^{\rm SC} = \lambda_{y'z'}^{(1)} T_{1z'}$ would reduce to the usual form[38] for the inverse DM interaction:

$$P_{1\alpha}^{\rm SC} = -\sqrt{2}\bar{\lambda}_\alpha^{(1)}\Big\{\mathbf{x}'\times\mathbf{T}_1\Big\}_\alpha, \tag{12}$$

with $\bar{\lambda}_{x'}^{(1)}=0$, $\bar{\lambda}_{y'}^{(1)} = \lambda_{y'z'}^{(1)}/\sqrt{2}$, and $\bar{\lambda}_{z'}^{(1)} = -\lambda_{z'y'}^{(1)}/\sqrt{2} = -\lambda_{y'z'}^{(1)}/(2\sqrt{2})$ so that $\bar{\lambda}_{z'}^{(1)} = -\bar{\lambda}_{y'}^{(1)}/2$.

The second SC-induced polarization is associated with the DM interaction D_2:

$$P_{2\alpha}^{\rm SC} = \lambda_\alpha^{(2)} T_{2\alpha}, \tag{13}$$

where $\mathbf{T}_2$ was defined by Eq.(5). As shown in Appendix B, the z' coefficient $\lambda_{z'}^{(2)}$ may differ from the x' and y' coefficients $\lambda_{x'}^{(2)} = \lambda_{y'}^{(2)}$.

For the simple tilted cycloid of Eqs.(6-8) in zero magnetic field,

$$\langle \mathbf{P}_1^{\rm SC}\rangle = 2\pi S^2\delta\cos\tau \left\{\frac{1}{\sqrt{2}}\Big(\lambda_{z'y'}^{(1)} - \frac{1}{2}\lambda_{y'z'}^{(1)}\Big)\mathbf{y}' - \lambda_{z'y'}^{(1)}\mathbf{z}'\right\}, \tag{14}$$

$$\langle \mathbf{P}_2^{\rm SC}\rangle = -\frac{3}{2}\lambda_{z'}^{(2)} S^2 \sin 2\tau\, \mathbf{z}'. \tag{15}$$

If the cycloid were not tilted, only the first SC polarization would be nonzero. When $c=d$, $\lambda_{z'y'}^{(1)} = \lambda_{y'z'}^{(1)}/2$ and the first term in $\langle \mathbf{P}_1^{\rm SC}\rangle$ along $\mathbf{y}'$ vanishes.

B. MS-induced polarizations

The first MS-induced polarization is produced by the uniform displacement of Fe with respect to O:

$$P_{1y'}^{\rm MS} = C_{1y'}\,\mathbf{y}'\cdot\mathbf{W}_1, \tag{16}$$

$$P_{1z'}^{\rm MS} = C_{1z'}\,\mathbf{z}'\cdot\mathbf{W}_1, \tag{17}$$

$$W_{1u} = \frac{1}{N}\sum_{\langle i,j\rangle^{\mathbf{u}}} \mathbf{S}_i\cdot\mathbf{S}_j. \tag{18}$$

It is easy to show that $\mathbf{x}'\cdot\mathbf{W}_1 = 0$. For a simple twisted cycloid,

$$\langle \mathbf{P}_1^{\rm MS}\rangle = -\sqrt{3}C_{1z'}S^2\cos^2\tau\,\mathbf{z}'. \tag{19}$$

The energy $-\mathbf{E}\cdot\mathbf{P}_1^{\rm MS}$ uniformly shifts all the nearest-neighbor interactions by $\Delta J_1 = C_{1z'}E_{z'}/\sqrt{3}$.

The second MS-induced polarization can be written[48]

$$\mathbf{P}_2^{\rm MS} = C_2\,\mathbf{z}'\times\mathbf{W}_2, \tag{20}$$

$$W_{2u} = \frac{1}{N}\sum_{\langle i,j\rangle\mathbf{u}} (-1)^{n_i}\,\mathbf{S}_i\cdot\mathbf{S}_j. \tag{21}$$

Unlike $\mathbf{W}_1$, $\mathbf{W}_2$ alternates sign from one hexagonal layer to the next. The cross product with $\mathbf{z}'$ in Eq.(20) ensures that $\mathbf{P}_2^{\rm MS}$ remains a polar vector[49]. For a simple tilted cycloid in zero field, $\langle\mathbf{W}_2\rangle = \langle\mathbf{P}_2^{\rm MS}\rangle = 0$. The energy $-\mathbf{E}\cdot\mathbf{P}_2^{\rm MS}$ shifts the nearest-neighbor exchange interaction J_1 by an amount proportional to C_2E. For example, the nearest-neighbor exchange between spins at $\mathbf{R}_i$ and $\mathbf{R}_i + a\mathbf{z}$ is shifted by $\Delta J_1 = (-1)^{n_i}C_2(E_x - E_y)/\sqrt{3}$. Appendix C shows that $C_2 = \sqrt{3}C_{1y'}$.

The MS-induced polarization associated with next-nearest neighbor sites can be similarly constructed starting with

$$W_{3u} = \frac{1}{2N}\sum_{(i,j)'\mathbf{u}} \mathbf{S}_i\cdot\mathbf{S}_j, \tag{22}$$

$$W_{4u} = \frac{1}{2N}\sum_{(i,j)'\mathbf{u}} (-1)^{n_i}\,\mathbf{S}_i\cdot\mathbf{S}_j, \tag{23}$$

where all next-nearest neighbor pairs $(i,j)'\mathbf{u}$ are double counted with $\mathbf{R}_j - \mathbf{R}_i = a\mathbf{v}$, $|\mathbf{v}| = \sqrt{2}$, and $\mathbf{v}\cdot\mathbf{u} = 0$. So for $\mathbf{u} = \mathbf{x}$, $\mathbf{v} = (0,1,1)$, $(0,1,-1)$, $(0,-1,1)$, and $(0,-1,-1)$. For next nearest neighbors, both $\mathbf{R}_i$ and $\mathbf{R}_j$ lie on either even or odd layers.

Since $\mathbf{x}'\cdot\mathbf{W}_3 = \mathbf{x}'\cdot\mathbf{W}_4 = 0$, the polarizations associated with $\mathbf{W}_3$ and $\mathbf{W}_4$ are

$$P_{3,4\,y'}^{\rm MS} = C_{3,4\,y'}\,\mathbf{y}'\cdot\mathbf{W}_{3,4}, \tag{24}$$

$$P_{3,4\,z'}^{\rm MS} = C_{3,4\,z'}\,\mathbf{z}'\cdot\mathbf{W}_{3,4}. \tag{25}$$

For a simple twisted cycloid,

$$\langle\mathbf{P}_3^{\rm MS}\rangle = 2\sqrt{3}S^2C_{3z'}\,\mathbf{z}' \tag{26}$$

while $\langle\mathbf{P}_4^{\rm MS}\rangle = 0$. The energy $-\mathbf{E}\cdot\mathbf{P}_3^{\rm MS}$ uniformly shifts all the next nearest-neighbor interactions by $\Delta J_2 = C_{3z'}E_{z'}/\sqrt{3}$.

Another possible MS-induced polarization is associated with the spin exchange ANI or different exchange couplings for different spin components $S_{i\alpha}$. Because it is of order δ^2, this polarization can be neglected.

C. ANI-induced polarizations

The ANI-induced polarization $\mathbf{P}^{\rm ANI} = \mathbf{P}_\perp^{\rm ANI} + \mathbf{P}_\parallel^{\rm ANI}$, which arises from the spin-dependent hybridization between the Fe ions and their ligands, contains components perpendicular or parallel to $\mathbf{z}'$. As shown in Appendix D, the perpendicular polarization $\mathbf{P}_\perp^{\rm ANI} = \mathbf{P}_\perp^{\rm ANI(1)} + \mathbf{P}_\perp^{\rm ANI(2)}$ has two sets of terms associated with the electric-field dependence of the local single-ion ANI axis $[\sin\theta_i\cos\phi_i, \sin\theta_i\sin\phi_i, \cos\theta_i]$ defined by Eq.(D1). The first set is produced by the dependence of the polar angle θ_i on the electric field $\mathbf{E}$:

$$\mathbf{P}_\perp^{\rm ANI(1)} = \frac{\xi_1}{4N}\sum_i \big(S_{ix'}\mathbf{x}' + S_{iy'}\mathbf{y}'\big)S_{iz'}, \tag{27}$$

which agrees with the first ANI-induced polarization proposed by deSousa *et al.* [48].

An additional perpendicular polarization

$$\frac{\xi_2}{4N}\sum_i\Big\{\big({S_{ix'}}^2 - {S_{iy'}}^2\big)\mathbf{y}' + 2S_{ix'}S_{iy'}\mathbf{x}'\Big\} \tag{28}$$

with $\xi_2 = \xi_1/(2\sqrt{2})$ was proposed in Ref.[48]. However, the cross terms $S_{i\beta}S_{i\gamma}$ $(\beta\neq\gamma)$ in Eq.(D5) cancel this contribution.

The second set of perpendicular ANI-induced terms is produced by the dependence of the azimuthal angle ϕ_i on $\mathbf{E}$:

$$\mathbf{P}_\perp^{\rm ANI(2)} = -\frac{3\xi_3}{N}\sum_i (-1)^{n_i}\big(S_{iy'}\mathbf{x}' - S_{ix'}\mathbf{y}'\big)S_{iz'}, \tag{29}$$

which was not previously proposed.

We also construct the ANI-induced polarization parallel to $\mathbf{z}'$ produced by the electric-field dependence of the constant K:

$$\mathbf{P}_\parallel^{\rm ANI} = \frac{\xi_4}{4N}\,\mathbf{z}'\sum_i {S_{iz'}}^2, \tag{30}$$

which shifts the single-ion ANI by $\Delta K = \xi_4 E_{z'}/4$. For a simple tilted cycloid in zero field, $\langle\mathbf{P}^{\rm ANI}\rangle = \xi_4 S^2\mathbf{z}'/8$ includes only a contribution from ξ_4 and is parallel to $\mathbf{z}'$.

D. Total induced polarization

With all proposed terms, the net induced polarization in the cycloidal phase is $\mathbf{P}^{\rm ind} = \mathbf{P}^{\rm SC} + \mathbf{P}^{\rm MS} + \mathbf{P}^{\rm ANI}$. For the simple tilted cycloid,

$$\langle\mathbf{z}'\cdot\mathbf{P}^{\rm ind}\rangle = S^2\Big\{-2\pi\lambda^{(1)}_{z'y'}\delta\cos\tau - \frac{3}{2}\lambda^{(2)}_{z'}\sin 2\tau + \frac{\xi_4}{8} - \sqrt{3}C_{1z'}\cos^2\tau + 2\sqrt{3}C_{3z'}\Big\}. \tag{31}$$

Of course, the components of $\langle\mathbf{P}^{\rm ind}\rangle$ perpendicular to $\mathbf{z}'$ do not change the magnitude of the total polarization significantly. The change in polarization from the paramagnetic phase above $T_{\rm N}$ to the cycloidal phase below $T_{\rm N}$ is given by Eq.(31). Recently, Lee *et al.* [7] observed that $\langle\mathbf{P}^{\rm ind}\rangle$ has a magnitude of about 400 nC/cm^2 and opposes $\mathbf{P}^{\rm FE}$ due to the suppressed displacement of the Fe ions compared to the Bi ions.

By comparison, the induced polarization of the canted AF evaluated using Eq.(9) is given by

$$\langle \mathbf{z}' \cdot \mathbf{P}^{\rm ind}_{\rm AF} \rangle = -S^2 \Big\{ 3\lambda^{(2)}_{z'} \sin 2\tau + \sqrt{3} C_{1z'} \cos 2\tau + 2\sqrt{3} C_{3z'} \Big\}, \quad (32)$$

which has no ANI contribution because the spins are in the $\{x', y'\}$ plane. So the change in polarization from the AF phase to the cycloidal phase at zero field is given by

$$\Delta \langle \mathbf{z}' \cdot \mathbf{P}^{\rm ind} \rangle = S^2 \Big\{ -2\pi \lambda^{(1)}_{z'y'} \delta \cos \tau + \frac{3}{2} \lambda^{(2)}_{z'} \sin 2\tau + \frac{\xi_4}{8} - \sqrt{3} C_{1z'} \sin^2 \tau \Big\}. \quad (33)$$

Despite an early measurement of 1 nC/cm^2 [4], the magnitude of the polarization change $\Delta \langle \mathbf{z}' \cdot \mathbf{P}^{\rm ind} \rangle$ below H_c extrapolated to zero field has recently been estimated as 40 nC/cm^2 [5,6].

The Hamiltonian in zero electric field can be simply written in terms of the induced polarizations as

$$\frac{1}{N}\mathcal{H} = -\frac{\sqrt{3} J_1}{C_{1z'}} \mathbf{z}' \cdot \mathbf{P}^{\rm MS}_1 - \frac{\sqrt{3} J_2}{C_{3z'}} \mathbf{z}' \cdot \mathbf{P}^{\rm MS}_3 + \frac{\sqrt{2} D_1}{\lambda^{(1)}_{z'y'}} \mathbf{z}' \cdot \mathbf{P}^{\rm SC}_1 + \frac{D_2}{\lambda^{(2)}_{z'}} \mathbf{z}' \cdot \mathbf{P}^{\rm SC}_2 - \frac{4K}{\xi_4} \mathbf{z}' \cdot \mathbf{P}^{\rm ANI} - \frac{2\mu_{\rm B} H}{N} \sum_i \mathbf{m} \cdot \mathbf{S}_i. \quad (34)$$

Introducing the field dependence of the DM interactions, we find $\lambda^{(1)}_{z'y'} = -\sqrt{2}\partial D_1/\partial E_{z'}$ and $\lambda^{(2)}_{z'} = -\partial D_2/\partial E_{z'}$. Similarly, $C_{1z'} = \sqrt{3}\,\partial J_1/\partial E_{z'}$, $C_{3z'} = \sqrt{3}\,\partial J_2/\partial E_{z'}$, and $\xi_4 = 4\partial K/\partial E_{z'}$.

All $\mathbf{z}'$ components of the induced polarization $\mathbf{P}^{\rm ind}$ appear in $\mathcal{H}$ above. Because $\mathbf{P}^{\rm FE}$ appears above $T_{\rm N}$ in the paramagnetic phase, each static magnetically-induced polarization along $\mathbf{z}'$ corresponds to a term in the Hamiltonian. Due to the symmetry lowering associated with $\mathbf{P}^{\rm FE}$, each bilinear spin term that appears in $\mathcal{H}$ also contributes to an induced polarization parallel to $\mathbf{P}^{\rm FE}$.

Taking $c = d$ in Eq.(14),

$$\langle \mathbf{P}^{\rm ind} \rangle = -\frac{1}{N} \frac{\partial \langle \mathcal{H} \rangle}{\partial \mathbf{E}} \quad (35)$$

has no components perpendicular to $\mathbf{z}'$. Components of the operator $\mathbf{P}^{\rm ind}$ perpendicular to $\mathbf{z}'$ would then contribute only to the transition matrix elements $\langle n \neq 0 | \mathbf{P}^{\rm ind} | 0 \rangle$. In other words, $\mathcal{H}$ includes all induced polarizations with static contributions $\langle 0 | \mathbf{P}^{\rm ind} | 0 \rangle$ but not induced polarizations with only dynamical contributions $\langle n \neq 0 | \mathbf{P}^{\rm ind} | 0 \rangle$. For example, $\mathbf{P}^{\rm MS}_2$ and $\mathbf{P}^{\rm MS}_4$ do not appear in $\mathcal{H}$ because $\langle \mathbf{P}^{\rm MS}_2 \rangle = \langle \mathbf{P}^{\rm MS}_4 \rangle = 0$.

We used Eq.(34) to check our numerical results for the matrix elements $\langle n | \mathbf{z}' \cdot \mathbf{P} | 0 \rangle$. Since $\langle n | \mathcal{H} | 0 \rangle = E_0 \delta_{n0}$, the appropriate sum of polarization matrix elements with the field-dependent term $-NH \langle n | \mathbf{m} \cdot \mathbf{M} | 0 \rangle$ must vanish when $n \neq 0$. We verified that this condition is indeed satisfied for all excited states and magnetic fields.

V. THZ ABSORPTION

The absorption of THz light is given by $\alpha(\omega) = (2\omega/c)\,{\rm Im} N(\omega)$ where[33,50]

$$N(\omega) \approx \sqrt{(\epsilon^{\infty}_{ii} + \chi^{ee}_{ii}(\omega))(1 + \chi^{mm}_{jj}(\omega))} \pm \chi^{me}_{ji}(\omega) \quad (36)$$

is the complex refractive index for a linearly polarized beam, $\underline{\chi}^{ee}$, $\underline{\chi}^{mm}$ and $\underline{\chi}^{me}$ are the dielectric, magnetic, and magnetoelectric susceptibility tensors describing the dynamical response of the spin system[31–34] and $\underline{\epsilon}^{\infty}$ is the background dielectric constant tensor associated with charge excitations at higher energies. Subscripts i and j refer to the electric and magnetic polarization directions, respectively. The second term, which depends on the light propagation direction and produces NDD, is separated from the mean absorption by writing $N(\omega) = \bar{N}(\omega) \pm \chi^{me}_{ji}(\omega)$.

Summing over the SW modes n at the cycloidal ordering wavevector $\mathbf{Q}$, $\Delta\alpha(\omega) = (4\omega/c)\,{\rm Im}\chi^{me}_{ji}(\omega)$ is given by

$$\Delta\alpha(\omega) = \sum_n A_n\, \delta(\omega - \omega_n), \quad (37)$$

$$A_n = NX\omega_n\, {\rm Re}\Big\{ \rho_{\rm n0} \mu_{0\rm n} \Big\}, \quad (38)$$

$$\rho_{0n} = \langle 0 | \mathbf{P}^{\rm ind} \cdot \mathbf{e}/\mathcal{V} | n \rangle, \quad (39)$$

$$\mu_{0n} = \langle 0 | \mathbf{M} \cdot \mathbf{h}/\mu_{\rm B} | n \rangle, \quad (40)$$

where $\mathcal{V} = a^3$ is the volume per Fe site, $\mathbf{P}^{\rm ind}/\mathcal{V}$ is given in units of nC/cm^2, and X is given in Appendix E. The THz electric and magnetic fields are polarized in the $\mathbf{e}$ and $\mathbf{h}$ directions, respectively.

After expanding $\bar{N}(\omega)$ for small susceptibilities, we find that $\bar{\alpha}(\omega) = (2\omega/c)\,{\rm Im}\bar{N}(\omega)$ is given by

$$\bar{\alpha}(\omega) = \sum_n B_n\, \delta(\omega - \omega_n), \quad (41)$$

$$B_n = N\omega_n \Big\{ Y_1 |\rho_{0n}|^2 + Y_2 |\mu_{0n}|^2 \Big\}, \quad (42)$$

where Y_1 and Y_2 are given in terms of the dielectric constant ϵ^{∞}_{ii} in Appendix E. Based on a fit to the interference fringes, we used $\epsilon^{\infty}_{ii} = 27.54$ and 51.55 for $\mathbf{e} = [1, 1, 0]$ and $\mathbf{e} = [1, -1, 0]$, respectively.

For each orientation of the static magnetic field and light polarization, the integrated weight of every spectroscopic peak at ω_n is compared with the measured values. This eliminates estimates of the individual peak widths. Because the polarization and magnetization matrix elements are generally complex with an arbitrary overall phase that differs for each mode n, we can choose

TABLE II: **Fitting parameters (nC/cm^2) from $\Delta\alpha$**

	$\lambda^{(1)}_{y'z'}$	$\lambda^{(1)}_{z'y'}$	$\lambda^{(2)}_{x'}$, $\lambda^{(2)}_{y'}$	$\lambda^{(2)}_{z'}$	$N_{\rm par}$	$\chi^2_{\rm min}$
fit 1	-82.0	-50.3	$+35.2$	$+13.6$	4	1.543
error	±3.1	±8.0	±1.9	±3.0		
fit 2	-78.7	-39.4	$+33.7$	$+13.9$	3	1.536
error	±3.5	±1.7	±1.9	±3.0		

$\langle 0|P_{z'}|n\rangle$ to be real. Other magnetization and polarization matrix elements for mode n are then either purely real or imaginary. Under reversal of the field orientation, our numerical results indicate that $\langle 0|\mathbf{M}|n\rangle \rightarrow -\langle 0|\mathbf{M}|n\rangle^\star$ and $\langle n|\mathbf{P}|0\rangle \rightarrow \langle n|\mathbf{P}|0\rangle^\star$. It follows that the NDD vanishes for zero field. Our numerical results also indicate that the NDD should vanish[51] for field directions $[0,0,1]$ and $[1,1,0]$.

Unfortunately, fitting results for the mean absorption $\bar{\alpha}(\omega)$ were markedly inferior to results for $\Delta\alpha(\omega)$. This may be caused by uncertainty about the dielectric constants ϵ^∞_{ii}, which does not enter $\Delta\alpha(\omega)$. Moreover, the measured *difference* between the absorption in positive and negative fields is much less prone to systematic experimental error than $\bar{\alpha}(\omega)$.

Experimental results for the NDD with field along $\mathbf{m} = [1,-1,0]$ are plotted in Figs.5(a) and (b) for $\mathbf{e} = [1,-1,0]$ and $[1,1,0]$, respectively. For some modes, the NDD is strong enough that $\alpha(\omega)$ is small for light traveling in one direction but large for light traveling in the other direction[37]. In particular, for $\Psi_0 \approx 15.5$ cm^{-1} and $\mathbf{e} = [1,1,0]$, $A_n = 0.67$ cm^{-2} for an 8 T field along $\mathbf{m} = [1,-1,0]$ and light propagating along $\mathbf{k} = [0,0,1]$ while $A_n = 4.12$ cm^{-2} when either $\mathbf{m}$ or $\mathbf{k}$ is reversed.

Fits to the NDD are based on the plotted 2, 4, 6, 8, 10, and 12 T data sets. For each field value with two light polarizations, we evaluate the integrated weights for the 8 modes Ψ_0, $\Phi^{(1)}_1$, $\Psi^{(1,2)}_1$, $\Phi^{(1,2)}_2$, and $\Psi^{(1,2)}_2$ between roughly 12 and 35 cm^{-1}. Hence, there are $N_{\rm dat} = 96$ data points for $\Delta\alpha(\omega)$. Because the $\Phi^{(1,2)}_2$ and $\Psi_0/\Phi^{(1)}_1$ pairs are nearly degenerate in small fields, the average predicted NDD of those pairs are compared with the measured values of $\Delta\alpha(\omega)$ in a 2 T field.

Remarkably, the NDD for $\mathbf{m} = [1,-1,0]$ is dominated by the two sets of SC polarizations $\mathbf{P}^{\rm SC}_1$ and $\mathbf{P}^{\rm SC}_2$ associated with the DM interactions D_1 and D_2, respectively. Neglecting MS and ANI leaves four polarization parameters: $\lambda^{(1)}_{y'z'}$, $\lambda^{(1)}_{z'y'}$, $\lambda^{(2)}_{x'} = \lambda^{(2)}_{y'}$, and $\lambda^{(2)}_{z'}$. The diagonal parameters $\lambda^{(1)}_{x'x'} = -\lambda^{(1)}_{y'y'} = c - d$ (domain 2) are obtained from $\lambda^{(1)}_{y'z'} = -2\sqrt{2}c$ and $\lambda^{(1)}_{z'y'} = -\sqrt{2}d$ using the relations in Appendix B.

Above about 12 T, agreement between the theoretical and experimental values for $\Delta\alpha$ begins to deteriorate. This failure may be caused by the avoided mode crossings between 12 and 16 T, which mix $\Psi^{(2)}_1$, $\Psi^{(1)}_1$, and $\Phi^{(1)}_2$ and are imperfectly captured by our model. Since each of those modes exhibits pronounced NDD, the fitted polarization parameters are very sensitive to the precise behavior of the modes at the avoided crossings.

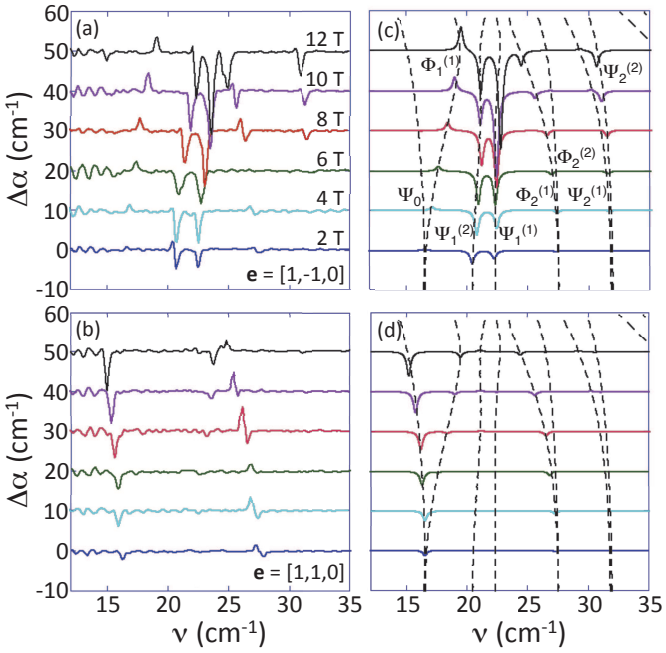

FIG. 5: (Color online) The measured (a,b) and predicted (c,d) NDD for 2 to 12 T fields along $\mathbf{m} = [1,-1,0]$ and for $\mathbf{e} = [1,-1,0]$ (a and c) or $[1,1,0]$ (b and d). Predictions are based on fit 2. Dashed curves in (c) and (d) are the predicted mode frequencies.

Based on the typical noise level for the absorption, we set the experimental uncertainty for the integrated NDD of each peak to $\sigma = 1$ cm^{-2}. The error bars for each polarization parameter are then obtained from the condition that $\chi^2/\chi^2_{\rm min}$ increases by[52] $1/(N_{\rm dat} - N_{\rm par} - 1)$.

The results for fit 1 in Table II with $N_{\rm par} = 4$ free parameters indicate that for domain 2, $\lambda^{(1)}_{x'x'} = -\lambda^{(1)}_{y'y'} \approx -6.6 \pm 6.7$ nC/cm^2. So our results imply the absence of the diagonal terms in $\underline{\lambda}^{(1)}$ and support the simplified form of Eq.(12) for the first SC-induced polarization. With a slightly smaller $\chi^2_{\rm min}$, fit 2 with $N_{\rm par} = 3$ takes $\lambda^{(1)}_{x'x'} = \lambda^{(1)}_{y'y'} = 0$ and $\lambda^{(1)}_{y'z'} = 2\lambda^{(1)}_{z'y'}$.

Because the sample $\mathbf{P}^{\rm FE}$ may point parallel or antiparallel to [1,1,1], the overall sign of $\Delta\alpha(\omega)$ and of the polarization parameters is ambiguous. According to Katsura *et al.*[38], however, $\bar{\lambda}_{z'} = -\lambda^{(1)}_{z'y'}/\sqrt{2}$ in Eq.(12) should be positive so that $\lambda^{(1)}_{z'y'} < 0$. This condition is used to fix the overall sign of the SC parameters in Table II.

Results for fit 2 are plotted in Figs.5(c) and (d). Although it underestimates the NDD for $\Phi^{(1)}_2$ when $\mathbf{e} = [1,1,0]$ (perhaps due to a small shift in the spectra $\alpha(\omega)$ for positive and negative fields), this fit otherwise describes all the relevant features of the NDD with field orientation $\mathbf{m} = [1,-1,0]$. Based on fit 2 parameters, the predicted SC polarizations $\langle \mathbf{P}^{\rm SC}_1 \rangle \approx 7.0\,\mathbf{z}'$ nC/cm^2

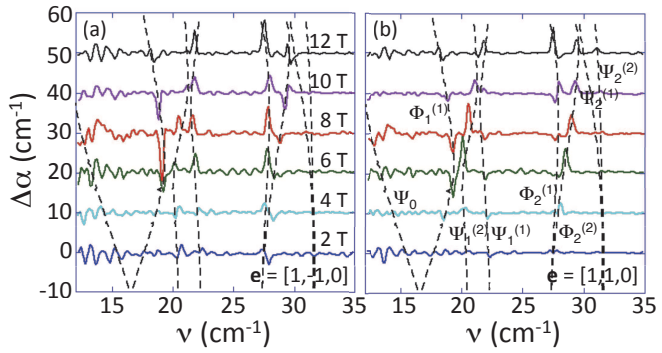

FIG. 6: (Color online) The measured NDD for 2 to 12 T fields along $\mathbf{m} = [1,1,0]$ and for $\mathbf{e} =$ (a) $[1,-1,0]$ or (b) $[1,1,0]$. Dashed curves are the predicted mode frequencies.

and $\langle \mathbf{P}_2^{\rm SC} \rangle \approx -2.1\,\mathbf{z}'$ nC/cm^2 point parallel and antiparallel to $\mathbf{P}^{\rm FE}$, respectively. Hence, the total SC-induced polarization points along $\mathbf{P}^{\rm FE}$ with a magnitude of 4.9 nC/cm^2. From Eq.(32), the SC-induced polarization of the canted AF above H_c is given by $-4.2\,\mathbf{z}'$ nC/cm^2 opposite to $\mathbf{P}^{\rm FE}$.

Since the MS-induced polarizations above and below H_c differ by $-\sqrt{3}S^2 C_{1z'} \sin^2\tau \approx 6.9\times10^{-4}\,C_{1z'}$, this term can be ignored in Eq.(33). Using the LSDA+U result [40] $\xi_4 \approx 110$ nC/cm^2, the change in $\langle \mathbf{z}'\cdot\mathbf{P}^{\rm ind}\rangle$ below H_c contains the ANI-induced contribution $S^2\xi_4/8 \approx 86$ nC/cm^2. Therefore, the total predicted change $\Delta\langle \mathbf{z}'\cdot\mathbf{P}^{\rm ind}\rangle \approx 96$ nC/cm^2 in the induced polarization from above to below H_c is more than twice larger than the recent experimental estimates of 40 nC/cm^2 [5,6]. Alternatively, fitting the experimental jump to Eq.(33) gives $\xi_4 = 40$ nC/cm^2, 40% smaller than the LSDA+U prediction.

A possible explanation for this discrepancy is that we have slightly overestimated D_2 and S_0. As mentioned above, taking $D_2 < 0.079$ meV or $S_0 < 0.185$ would stabilize a canted AF phase with spins tilted out of the $\{x',y'\}$ plane. Because such a state would recoup some ANI energy, the predicted jump in the induced polarization at H_c would be reduced. The planar canted AF phase of Eq.(9) would then appear above some higher critical field $H_c' > H_c$. Due to the non-coplanar AF phase, the lower AF mode α in Fig.4 would decrease with field between H_c and H_c', vanish at H_c', and increase with field only above H_c'.

Using $\lambda^{(1)}_{z'y'} = -\sqrt{2}\partial D_1/\partial E_{z'}$ and $\lambda^{(2)}_{z'} = -\partial D_2/\partial E_{z'}$, the results of fit 2 for $\lambda^{(1)}_{z'y'}$ and $\lambda^{(2)}_{z'}$ can be used to evaluate the dependence of D_1 and D_2 on an electric field applied along $\mathbf{z}'$. Raman measurements[17] indicate that the spectroscopic modes exhibit significant dependence on an electric field of 75 kV/cm along [0,1,0]. For an electric field of 100 kV/cm along [1,1,1], we find $\Delta D_1/D_1 = 6.0\times10^{-3}$ and $\Delta D_2/D_2 = -6.4\times10^{-3}$. Although very small, the change in D_1 will slightly increase the size of δ and reduce the period of the cycloid. The change in D_2 will slightly reduce the tilt angle τ.

VI. DISCUSSION

Although the distorted cycloid of $BiFeO_3$ is produced by the competition between magnetic interactions, the SC polarization dominates the NDD of $BiFeO_3$. The NDD of $BiFeO_3$ along $\mathbf{m} = [1,-1,0]$ is well described by our model. Due to the pronounced NDD for Ψ_0 when $\mathbf{e} = [1,1,0]$, $BiFeO_3$ may be used as an optical diode, transparent to light traveling in one direction but opaque for light traveling in the opposite direction. Despite the successes of this model, several issues must be addressed.

For light propagating along $\mathbf{k} = [0,0,\pm1]$, symmetry arguments[51] and our numerical results indicate that NDD should be absent for $\mathbf{m} = [\eta,\eta,\kappa]$ with stable domain 1 if either $\mathbf{e}$ or $\mathbf{h}$ coincides with $\mathbf{x}_1'$. Even for $\mathbf{m} = [1,1,1]$, where all three domains are degenerate[39], the NDD should vanish if domains 2 and 3 are equally populated. While NDD is not observed for $\mathbf{m} = [0,0,1]$, the NDD for $\mathbf{m} = [1,1,0]$ is plotted in Fig.6. The most pronounced NDD is seen near the avoided mode crossing of $\Psi_1^{(2)}$ and $\Phi_1^{(1)}$ around 8 T.

To estimate the relative sizes of the NDD in fields along $[1,1,0]$ and $[1,-1,0]$, we calculate the net squared NDD,

$$\Omega = \frac{1}{N_{\rm dat}\,\sigma^2}\sum_n {A_n}^2, \tag{43}$$

where the sum runs over all modes between 2 and 12 T and A_n was defined by Eq.(37). Since $\Omega = 3.50$ and 9.45, respectively, the observed NDD is substantially weaker for $[1,1,0]$ than for $[1,-1,0]$. Because the contributions from metastable domains 2 and 3 cancel each other, they can not explain the NDD observed for $\mathbf{m} = [1,1,0]$. While a population imbalance between metastable domains 2 and 3 would produce very weak NDD, domain 1 is expected to predominate above a few Tesla. Misalignment of the crystal could produce the observed NDD when $\mathbf{m} = [1,1,0]$ but the excellent agreement between the measured and predicted mode spectrum in Fig.4(b) suggests that the sample is aligned quite well.

The NDD for $\mathbf{m} = [1,1,0]$ probably arises from an optical misalignment[53] with the polarization vectors $\mathbf{e}$ and $\mathbf{h}$ rotated about $\mathbf{k} = [0,0,1]$. For $\mathbf{m} = [\eta,\eta,\kappa]$, $\Omega(\alpha) \approx \Omega(\pi/4)\sin^2(2\alpha)$, where α is the angle between $\mathbf{e}$ and $[1,-1,0]$. As shown in Fig.7 for $\mathbf{m} = [1,1,0]$ and $[0,0,1]$, $\Omega(\alpha)$ peaks at $\alpha = \pi/4$, i.e. when $\mathbf{e} = [1,0,0]$ and $\mathbf{h} = [0,1,0]$ or $\mathbf{e} = [0,1,0]$ and $\mathbf{h} = [-1,0,0]$. For $\mathbf{m} = [1,-1,0]$, $\Omega(\alpha) \approx \Omega(0) - (\Omega(0)/2)\sin^2(2\alpha)$ is predicted to drop to about $\Omega(0)/2$ at $\alpha = \pi/4$. Note that the squared NDD for an individual mode does not obey these relations: they are obeyed only by the net squared NDD summed over all modes. Measuring the NDD while rotating the THz polarization vectors about $[0,0,1]$ would help resolve questions about the NDD when $\mathbf{m} = [1,1,0]$.

While the SC dominates the dynamical response of $BiFeO_3$, MS dominates its static properties. As argued

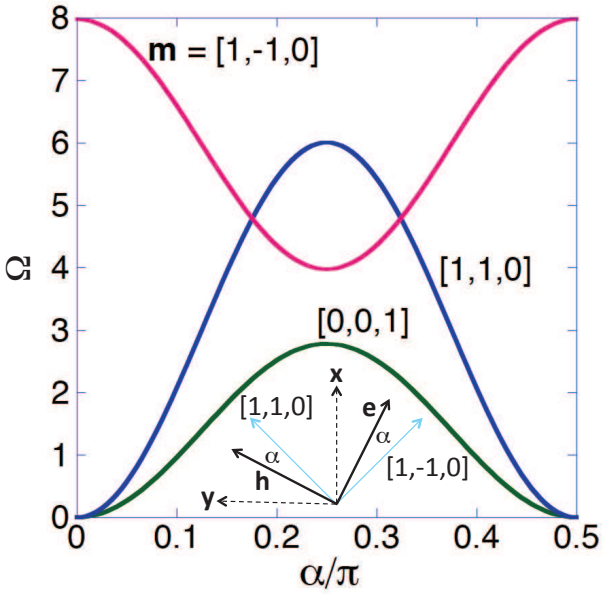

FIG. 7: (Color online) The predicted Ω versus α for fields along $[1,-1,0]$ (red), $[1,1,0]$ (blue), and $[0,0,1]$ (green). SC parameters are obtained from fit 2. Inset shows the rotation of $\mathbf{e}$ and $\mathbf{h}$ about $[0,0,1]$.

elsewhere[54], $\langle \mathbf{P}_1^{\rm MS}\rangle \approx -\sqrt{3}S^2 C_{1z'}\mathbf{z}'$ dominates the induced polarization and opposes $\mathbf{P}^{\rm FE}$ below $T_{\rm N}$, in agreement with recent measurements[7]. A unified model of ferroelectricity[55,56] also concludes that SC and ANI make minor contributions to $\langle \mathbf{P}^{\rm ind}\rangle$ compared to MS.

The distinction between static and dynamics properties in $BiFeO_3$ is not surprising. Since spin fluctuations $\delta\mathbf{S}_i$ are transverse to the almost collinear, cycloidal spin state $\langle \mathbf{S}_i\rangle$, we find that $\delta\mathbf{S}_i \times \langle \mathbf{S}_j\rangle \neq 0$ but $\delta\mathbf{S}_i \cdot \langle \mathbf{S}_j\rangle \approx 0$ for nearby sites i and j. Because the ANI is $BiFeO_3$ is extremely weak, spin fluctuations more strongly affect the SC-induced polarization than the MS- and ANI-induced polarizations. By contrast, the almost collinear spin structure of $BiFeO_3$ efficiently produces a static polarization through the MS and ANI but not through the SC since $\langle \mathbf{S}_i\rangle \cdot \langle \mathbf{S}_j\rangle \neq 0$ and $(1/N)\sum_i \langle S_{iz'}\rangle\langle S_{iz'}\rangle \neq 0$ but $\langle \mathbf{S}_i\rangle \times \langle \mathbf{S}_j\rangle \approx 0$.

Tokunaga *et al.*[57] recently attributed the induced *transverse* polarization along $\mathbf{y}'$ to the first SC polarization $\mathbf{P}_1^{\rm SC}$ with $\underline{\lambda}^{(1)}$ matrix elements $\lambda^{(1)}_{z'y'}$ and $\lambda^{(1)}_{y'y'}$. Those authors found that $|\lambda^{(1)}_{y'y'}| \approx 104$ nC/cm^2 and $|\lambda^{(1)}_{z'y'}| \approx 73$ nC/cm^2. By contrast, fit 1 indicates that $|\lambda^{(1)}_{y'y'}| \approx 6$ nC/cm^2 is very small. The result $|\lambda^{(1)}_{z'y'}|$ from Ref.[57] is reasonably close to the result $|\lambda^{(1)}_{z'y'}| \approx 50 \pm 8$ nC/cm^2 from fit 1.

Considering only the first set of SC terms associated with D_1, earlier work[27] identified $\Psi_1^{(1)}$ as an electromagnon[58,59] that can be excited by a THz electric field when $\mathbf{H} = 0$. When both sets of SC terms are considered, $\Psi_0/\Phi_1^{(1)}$ and $\Phi_2^{(1,2)}$ also become electrically active at zero field. Of the four modes observed in zero field, only $\Psi_1^{(2)}$ at 20.4 cm^{-1} is not electrically active. Using the SC parameters in Table II, $\Psi_1^{(1)}$ couples most strongly of all modes to a THz electric field for domains 2 and 3. This mode also exhibits the strongest NDD for nonzero field.

To summarize, the SC polarization matrix elements dominate the NDD in $BiFeO_3$. But work remains to understand the origin of the MS-induced and perpendicular polarizations in this important material. Our explanations for the jump in the induced polarization at H_c and for the observed weak NDD when $\mathbf{m} = [1,1,0]$ need to be confirmed. Nevertheless, we believe that the present work on $BiFeO_3$ provides a compelling example of how a quantitative microscopic theory of magnetoelectric couplings follows from an analysis of the observed dynamical magnetoelectric response based on an effective spin model supplemented by first-principles calculations.

We acknowledge helpful conversations with Eric Bousquet and Rogerio deSousa. We also thank Hee Taek Yi and Sang-Wook Cheong for preparation of the $BiFeO_3$ sample. Research sponsored by the Department of Energy, Office of Science, Basic Energy Sciences, Materials Sciences and Engineering Division (RF and JL) and by the Hungarian Research Funds OTKA K 108918, OTKA PD 111756, and Bolyai 00565/14/11(SB and IK). TR and UN acknowledge support by the Estonian Ministry of Education and Research Grant IUT23-03 and by the Estonian Science Foundation Grant ETF8703.

Appendix A: Experimental Details

A single ferroelectric domain $BiFeO_3$ sample with face area 7 mm^2 $(0,0,1)$ and thickness $d = 0.37$ mm along $[0,0,1]$ was grown at Rutgers University. Voigt measurements ($\mathbf{k} \perp \mathbf{m}$) up to 17 T were performed in Tallinn. Faraday ($\mathbf{k} \parallel \mathbf{m}$) measurements up to 12 T were performed in Tallinn and up to 31 T in Nijmegen, as reported earlier[19].

The Tallinn laboratory uses a Martin-Puplett type interferometer with a Si bolometer operating at 0.3 K and a mercury arc light source. Light pipes direct light to the sample in a He exchange gas-filled sample chamber placed into the cold 52 mm bore of a vertical-field superconducting 17 T solenoid. In the Voigt configuration, mirrors before and after the sample change the light direction perpendicular to $\mathbf{m}$. A rotatable wire grid on the dielectric substrate polarizer is placed before the first mirror. The sample can be rotated about the axis parallel to the direction of light propagation. A set of low pass filters with different cut-off frequencies is situated on the filter wheel in liquid He between the sample chamber and the bolometer chamber below the solenoid.

Applying a 17 T field at 4 K for tens of minutes populates magnetic domain 1 when $\mathbf{m} = [1,1,0]$ or domains 2 and 3 when $\mathbf{m} = [1,-1,0]$ [19]. Spectra were then measured in different $\pm\mathbf{H}$ fields for about 15 minutes per

field. No change in the magnetic domain populations was observed when a −17 T field was applied after a +17 T field.

The zero-field absorption spectrum was subtracted from the spectra measured in field, thereby canceling out diffraction and interference effects caused by the sample. The differential absorption coefficient is $\alpha(H) - \alpha(0) = -\ln(I_H/I_0)/d$, where I_0 and I_H are light intensity spectra in zero and H field and d is the sample thickness. Negative peaks in the differential absorption spectra for all field values were used to calculate the zero-field spectrum. To generate the field-dependent spectra, the calculated zero-field spectrum was aNDDed to the differential spectra. The NDD spectra $\Delta\alpha = \alpha(\mathbf{H}) - \alpha(-\mathbf{H})$ do not depend on the zero-field spectra.

Appendix B: SC-induced polarizations

The D_1 term in the Hamiltonian can be written

$$V_1^{\mathrm{SC}} = \sum_{u,\langle i,j\rangle^{\mathbf{u}}} \mathbf{F}^{(u)} \cdot (\mathbf{S}_i \times \mathbf{S}_j). \tag{B1}$$

In the absence of an electric field,

$$\mathbf{F}^{(x)} = \frac{D_1}{\sqrt{3}}(0, 1, -1), \tag{B2}$$

$$\mathbf{F}^{(y)} = \frac{D_1}{\sqrt{3}}(-1, 0, 1), \tag{B3}$$

$$\mathbf{F}^{(z)} = \frac{D_1}{\sqrt{3}}(1, -1, 0) \tag{B4}$$

along $\mathbf{x}$, $\mathbf{y}$, and $\mathbf{z}$, respectively. The polarization associated with D_1 is then

$$\begin{aligned} P_{1\alpha}^{\mathrm{SC}} &= -\frac{1}{N}\frac{\partial V_1^{\mathrm{SC}}}{\partial E_\alpha} \\ &= \frac{1}{N}\sum_{u,\langle i,j\rangle^{\mathbf{u}},\beta} \Pi_{\alpha\beta}^{(u)} \, (\mathbf{S}_i \times \mathbf{S}_j)_\beta, \end{aligned} \tag{B5}$$

where $\Pi_{\alpha\beta}^{(u)} = -\partial F_\beta^{(u)}/\partial E_\alpha$. LSDA+$U$ calculations[40] reveal that

$$\underline{\Pi}^{(x)} = \begin{pmatrix} 0 & -d & d \\ 0 & -c & -c \\ 0 & c & c \end{pmatrix}, \tag{B6}$$

$$\underline{\Pi}^{(y)} = \begin{pmatrix} c & 0 & c \\ d & 0 & -d \\ -c & 0 & -c \end{pmatrix}, \tag{B7}$$

$$\underline{\Pi}^{(z)} = \begin{pmatrix} -c & -c & 0 \\ c & c & 0 \\ -d & d & 0 \end{pmatrix}. \tag{B8}$$

Consequently, $\partial\mathbf{F}^{(u)}/\partial E_\alpha$ is not parallel to $\mathbf{F}^{(u)}$.

In the lab reference frame $\{x, y, z\}$, regrouping terms for domain 2 yields $P_{1\alpha}^{\mathrm{SC}} = \sum_\beta \Lambda_{\alpha\beta}^{(1)} T_{1\beta}$ with $\underline{\Lambda}^{(1)} = \underline{\Pi}^{(x)} - \underline{\Pi}^{(z)}$ or

$$\underline{\Lambda}^{(1)} = \begin{pmatrix} c & c-d & d \\ -c & -2c & -c \\ d & c-d & c \end{pmatrix}. \tag{B9}$$

We transform this matrix into the cycloidal reference frame $\{x', y', z'\}$ using the unitary matrix $\underline{U}$ for domain 2:

$$\underline{U} = \begin{pmatrix} 1/\sqrt{2} & 0 & -1/\sqrt{2} \\ -1/\sqrt{6} & \sqrt{2/3} & -1/\sqrt{6} \\ 1/\sqrt{3} & 1/\sqrt{3} & 1/\sqrt{3} \end{pmatrix} \tag{B10}$$

so that

$$\begin{aligned} \underline{\lambda}^{(1)} &= \underline{U}\,\underline{\Lambda}^{(1)}\,\underline{U}^{-1} \\ &= \begin{pmatrix} c-d & 0 & 0 \\ 0 & d-c & -2\sqrt{2}c \\ 0 & -\sqrt{2}d & 0 \end{pmatrix}. \end{aligned} \tag{B11}$$

The diagonal terms change sign for domains 1 and 3.

The D_2 term in the Hamiltonian can be written $V_2^{\mathrm{SC}} = D_2 N\, \mathbf{z}' \cdot \mathbf{T}_2$. Thus, the SC-induced polarization associated with D_2 can be generally written $P_{2\alpha}^{\mathrm{SC}} = \sum_\beta \Lambda_{\alpha\beta}^{(2)} T_{2\beta}$. In the lab reference frame, $\underline{\Lambda}^{(2)}$ is given by[40]

$$\underline{\Lambda}^{(2)} = \begin{pmatrix} e & f & f \\ f & e & f \\ f & f & e \end{pmatrix}. \tag{B12}$$

Transforming into the cycloidal reference frame,

$$\underline{\lambda}^{(2)} = \underline{U}\,\underline{\Lambda}^{(2)}\,\underline{U}^{-1} = \begin{pmatrix} e-f & 0 & 0 \\ 0 & e-f & 0 \\ 0 & 0 & e+2f \end{pmatrix} \tag{B13}$$

for all three domains. So $\underline{\lambda}^{(2)}$ is diagonal with components $\lambda_{x'}^{(2)} = \lambda_{y'}^{(2)} = e - f$ and $\lambda_{z'}^{(2)} = e + 2f$.

Appendix C: MS-induced polarizations

The MS-induced polarizations are $P_{1\alpha}^{\mathrm{MS}} = \sum_\beta \Gamma_{\alpha\beta}^{(1)} W_{1\beta}$ and $P_{2\alpha}^{\mathrm{MS}} = \sum_\beta \Gamma_{\alpha\beta}^{(2)} W_{2\beta}$. According to LSDA+$U$ calculations[40], $\underline{\Gamma}^{(i)}$ are given in the lab reference frame by

$$\underline{\Gamma}^{(1)} = \begin{pmatrix} g & h & h \\ h & g & h \\ h & h & g \end{pmatrix}, \tag{C1}$$

$$\underline{\Gamma}^{(2)} = \begin{pmatrix} 0 & -j & j \\ j & 0 & -j \\ -j & j & 0 \end{pmatrix}, \tag{C2}$$

where $j = g - h$. Transforming into the cycloidal reference frame,

$$\underline{U}\,\underline{\Gamma}^{(1)}\,\underline{U}^{-1} = \begin{pmatrix} j & 0 & 0 \\ 0 & j & 0 \\ 0 & 0 & g+2h \end{pmatrix}, \tag{C3}$$

$$\underline{U}\,\underline{\Gamma}^{(2)}\,\underline{U}^{-1} = \begin{pmatrix} 0 & -\sqrt{3}j & 0 \\ \sqrt{3}j & 0 & 0 \\ 0 & 0 & 0 \end{pmatrix} \tag{C4}$$

for all three domains. It follows that $C_{1y'} = j$, $C_{1z'} = g + 2h$, and $C_2 = \sqrt{3}j$. Therefore, $C_{1y'} = C_2/\sqrt{3}$.

Appendix D: ANI-induced polarizations

The perpendicular ANI-induced polarization $\mathbf{P}_{\perp}^{\rm ANI}$ is associated with the dependence of the polarization direction $\mathbf{n}$ on an electric field. The ANI energy is given by $V^{\rm ANI} = -K\sum_i(\mathbf{S}_i\cdot\mathbf{n}_i)^2$, where

$$\mathbf{n}_i = [\sin\theta_{iz}\cos\phi_{iz}, \sin\theta_{iz}\sin\phi_{iz}, \cos\theta_{iz}] \tag{D1}$$

is the local single-ion ANI axis and $\theta_{iz} = \cos^{-1}(\mathbf{n}_i\cdot\mathbf{z})$. Consequently,

$$P_z^{\rm ANI} = -\frac{1}{N}\frac{dV^{\rm ANI}}{dE_z} = -\frac{1}{N}\sum_i\Big\{\frac{\partial V^{\rm ANI}}{\partial\theta_{iz}}\frac{\partial\theta_{iz}}{\partial E_z} + \frac{\partial V^{\rm ANI}}{\partial\phi_{iz}}\frac{\partial\phi_{iz}}{\partial E_z}\Big\} - \frac{1}{N}\frac{\partial V^{\rm ANI}}{\partial K}\frac{\partial K}{\partial E_z}, \tag{D2}$$

which must be evaluated in the limit $\mathbf{n}_i \to \mathbf{z}'$.

Due to the rhombohedral crystal structure of $BiFeO_3$, $\partial\theta_{ix}/\partial E_x = \partial\theta_{iy}/\partial E_y = \partial\theta_{iz}/\partial E_z$ where $\theta_{ix} = \cos^{-1}(\mathbf{n}_i\cdot\mathbf{x})$ and $\theta_{iy} = \cos^{-1}(\mathbf{n}_i\cdot\mathbf{y})$. Similar identities hold for $\phi_{i\alpha}$. It follows that

$$P_x^{\rm ANI} = -\frac{1}{N}\frac{dV^{\rm ANI}}{dE_x} = -\frac{1}{N}\sum_i\Big\{\frac{\partial V^{\rm ANI}}{\partial\theta_{ix}}\frac{\partial\theta_{ix}}{\partial E_x} + \frac{\partial V^{\rm ANI}}{\partial\phi_{ix}}\frac{\partial\phi_{ix}}{\partial E_x}\Big\} - \frac{1}{N}\frac{\partial V^{\rm ANI}}{\partial K}\frac{\partial K}{\partial E_x} \tag{D3}$$

and

$$P_y^{\rm ANI} = -\frac{1}{N}\frac{dV^{\rm ANI}}{dE_y} = -\frac{1}{N}\sum_i\Big\{\frac{\partial V^{\rm ANI}}{\partial\theta_{iy}}\frac{\partial\theta_{iy}}{\partial E_y} + \frac{\partial V^{\rm ANI}}{\partial\phi_{iy}}\frac{\partial\phi_{iy}}{\partial E_y}\Big\} - \frac{1}{N}\frac{\partial V^{\rm ANI}}{\partial K}\frac{\partial K}{\partial E_y}. \tag{D4}$$

The first terms in Eqs.(D2-D4) produce the $\xi_1 = -4\sqrt{6}\,K\,\partial\theta_{iz}/\partial E_z$ polarization perpendicular to $\mathbf{z}'$. Because $\partial\phi_{i\alpha}/\partial E_\alpha$ is modulated by $(-1)^{n_i}$, the second terms produce the $\xi_3 = (2K/3)(-1)^{n_i}\,\partial\phi_{iz}/\partial E_z$ polarization, also perpendicular to $\mathbf{z}'$. The final terms produce the $\xi_4 = 4\sqrt{3}\,\partial K/\partial E_z$ polarization $\mathbf{P}_{\parallel}^{\rm ANI}$ along $\mathbf{z}'$.

In the lab reference frame, the perpendicular polarizations produced by the dependence of the polar and azimuthal angles θ_i and ϕ_i on the electric field $\mathbf{E}$ are given respectively by

$$(\mathbf{P}_{\perp}^{\rm ANI(1)})_\alpha = \frac{\xi_1}{12\sqrt{3}N}\sum_{i,\beta\gamma}\big(S_{i\alpha} - S_{i\beta}\big)S_{i\gamma}, \tag{D5}$$

$$(\mathbf{P}_{\perp}^{\rm ANI(2)})_\alpha = \frac{\xi_3}{2N}\sum_{i,\beta\gamma\delta}(-1)^{n_i}\epsilon_{\alpha\beta\gamma}\big(S_{i\beta} - S_{i\gamma}\big)S_{i\delta}. \tag{D6}$$

In the cycloidal reference frame, these polarizations are given by Eqs.(27) and (29).

Appendix E: Absorption parameters

The parameters that enter the THz absorption $\alpha(\omega)$ are

$$X = \frac{4\pi\mu_{\rm B}}{\hbar}\frac{\rm nC}{\rm cm^2} = \frac{0.1388}{\rm cm}, \tag{E1}$$

$$Y_1 = \frac{\pi\mathcal{V}}{\hbar c\epsilon_0\sqrt{\epsilon_{ii}^{\infty}}}\frac{\rm nC^2}{\rm cm^4} = \frac{6.975\times10^{-4}}{\sqrt{\epsilon_{ii}^{\infty}}\,\rm cm}, \tag{E2}$$

$$Y_2 = \frac{\pi\mu_{\rm B}^2\mu_0\sqrt{\epsilon_{ii}^{\infty}}}{\hbar c\mathcal{V}} = \frac{1.727\sqrt{\epsilon_{ii}^{\infty}}}{\rm cm}. \tag{E3}$$

Notice that $X = 4\sqrt{Y_1Y_2}$.

Appendix F: First-principles calculations

First-principles calculations were performed using density-functional theory (DFT) as implemented by the VASP code with an additional Hubbard (LSDA+U) interaction for the exchange-correlation functional. The Hubbard $U = 5$ eV and exchange $J_{\rm H} = 0$ eV were optimized[23,60] for Fe^{3+} in $BiFeO_3$. Projector augmented wave (PAW) potentials[61,62] were used. Integration over the Brillouin zone was performed using a supercell of 2×2×2 perovskite units (40 atoms, 8 f.u.) with a 3×3×3 Monkhorst-Pack (MP) k-points mesh. Wave functions were expanded in plane waves up to a 500 eV energy cutoff. The exchange interactions J_1 and J_2 were calculated using four different magnetic configurations (G-AFM, C-AFM, A-AFM and FM). The DM interactions D_1 and D_2 were evaluated using a 4×2×2 (80 atoms, 16

f.u.) supercell with a 1×3×3 MP mesh, replacing[60] all except four Fe^{3+} cations with Al^{3+}.

Derivatives of the exchange, DM, and ANI interactions with respect to an applied electric field E_α were calculated from the lowest-frequency polar eigenvector of the dynamical matrix by forcibly moving the atoms incrementally from the ground state ($R3c$) structure. The energy difference between the two structures was then divided by the induced electric polarization $P_\alpha^{\rm ind}$. The Fe-O-Fe bond angle was primarily responsible for the different polar eigenvectors obtained from the dynamic and force-constant matrices. While the eigenvector of the dynamic matrix decreases the bond-angle, the eigenvector of the force-constant matrix increases that angle. Due to those opposing tendencies, distinct behaviors were found for dynamic and static electric fields[40].

[1] J.R. Teague, R. Gerson, and W.J. James, Solid State Commun. **8**, 1073 (1970).
[2] I. Sosnowska, T. Peterlin-Neumaier, and E. Steichele, J. Phys. C: Solid State Phys. **15**, 4835 (1982).
[3] D. Lebeugle, D. Colson, A. Forget, and M. Viret, Appl. Phys. Lett. **91**, 022907 (2007).
[4] A.M. Kadomtseva, A.K. Zvezdin, Yu.F. Popv, A.P. Pyatakov, and G.P. Vorob'ev, JTEP Lett. **79**, 571 (2004).
[5] M. Tokunaga, M. Azuma, and Y. Shimakawa, J. Phys. Soc. Jpn. **79**, 064713 (2010).
[6] J. Park, S.-H. Lee, S. Lee, F. Gozzo, H. Kimura, Y. Noda, Y.J. Choi, V. Kiryukhin, S.-W. Cheong, Y. Jo, E.S. Choi, L. Balicas, G.S. Jeon, and J.-G. Park, J. Phys. Soc. Jpn. **80**, 114714 (2011).
[7] S. Lee, M.T. Fernandez-Diaz, H. Kimura, Y. Noda, D.T. Adroja, S. Lee, J. Park, V. Kiryukhin, S.-W. Cheong, M. Mostovoy, and J.-G. Park, Phys. Rev. B **88**, 060103 (2013).
[8] D. Lebeugle, D. Colson, A. Forget, M. Viret, A.M. Bataille, and A. Gukasov, Phys. Rev. Lett. **100**, 227602 (2008).
[9] M. Ramazanoglu, W. Ratcliff II, Y.J. Choi, S. Lee, S.-W. Cheong, and V. Kiryukhin, Phys. Rev. B **83**, 174434 (2011).
[10] J. Herrero-Albillos, G. Catalan, J.A. Rodriguez-Velamazan, M. Viret, D. Colson, and J.F. Scott, J. Phys.: Condens. Matter **22**, 256001 (2010).
[11] I. Sosnowska and R. Przenioslo, Phys. Rev. B **84**, 144404 (2011).
[12] S. Lee, W.M. Ratcliff II, S.-W. Cheong, and V. Kiryukhin, Appl. Phys. Lett. **92**, 192906 (2008); S. Lee. T. Choi, W. Ratcliff II, R. Erwin, S.-W. Cheong, and V. Kiryukhin, Phys. Rev. B **78**, 100101(R) (2008).
[13] J. Jeong, E.A. Goremychkin, T. Guidi, K. Nakajima, G.S. Jeon, S.-A. Kim, S. Furukawa, Y.B. Kim, S. Lee, V. Kiryukhin, S.-W. Cheong, and J.-G. Park, Phys. Rev. Lett. **108**, 077202 (2012).
[14] M. Matsuda, R.S. Fishman, T. Hong, C.H. Lee, T. Ushiyama, Y. Yanagisawa, Y. Tomioka, and T. Ito, Phys. Rev. Lett. **109**, 067205 (2012).
[15] Z. Xu, J. Wen, T. Berlijn, P.M. Gehring, C. Stock, M.B. Stone, W. Ku, G. Gu, S.M. Shapiro, R.J. Birgeneau, and G. Xu, Phys. Rev. B **86**, 174419 (2012).
[16] M. Cazayous, Y. Gallais, A. Sacuto, R. deSousa, D. Lebeugle, and D. Colson, Phys. Rev. Lett. **101**, 037601 (2008).
[17] P. Rovillain, R. de Sousa, Y. Gallais, A. Sacuto, M.A. Méasson, D. Colson, A. Forget, M. Bibes, A. Barthélémy. and M. Cazayous, Nat. Mat. **9**, 975 (2010).
[18] D. Talbayev, S.A. Trugman, S. Lee, H.T. Yi, S.-W. Cheong, and A.J. Taylor, Phys. Rev. B **83**, 094403 (2011).
[19] U. Nagel, R.S. Fishman, T. Katuwal, H. Engelkamp, D. Talbayev, H.T. Yi, S.-W. Cheong, and T. Rõõm, Phys. Rev. Lett. **110**, 257201 (2013).
[20] I. Sosnowska and A.K. Zvezdin, J. Magn. Magn. Mat. **140-144**, 167 (1995).
[21] A.P. Pyatakov and A.K. Zvezdin, Eur. Phys. J. B **71**, 419 (2009).
[22] K. Ohoyama, S. Lee, S. Yoshii, Y. Narumi, T. Morioka, H. Nojiri, G.S. Jeon, S.-W. Cheong, and J.-G. Park, J. Phys. Soc. Jpn. **80**, 125001 (2011).
[23] C. Ederer and N.A. Spaldin, Phys. Rev. B **71**, 060401(R) (2005).
[24] M. Ramazanoglu, M. Laver, W. Ratcliff II, S.M. Watson, W.C. Chen, A. Jackson, K. Kothapalli, S. Lee, S.-W. Cheong, and V. Kiryukhin, Phys. Rev. Lett. **107**, 207206 (2011).
[25] In previous work[14], the SW frequencies were scaled by $\sqrt{S(S+1)}$. This artificial introduction of quantum fluctuations made it awkward to obtain the correct SW frequencies of the canted AF phase, where the upper mode frequency is proportional to $2\mu_{\rm B}H$ rather than $2\mu_{\rm B}\sqrt{(S+1)/S}H$. In the present work, the frequencies are scaled by S. Consequently, the Heisenberg interactions increase from $J_1 = -4.50$ meV and $J_2 = -0.20$ meV to $J_1 = -5.32$ meV and $J_2 = -0.24$ meV. This rescaling was also applied to the quoted values of D_1 and K in Ref.[26]. Also keep in mind that we have redefined D_1 to be $\sqrt{2}$ larger than in earlier work.
[26] J. Jeong, M.D. Le, P. Bourges, S. Petit, S. Furukawa, S.-A. Kim, S. Lee, S.-W. Cheong, and J.-G. Park, Phys. Rev. Lett. **113**, 107202 (2014).
[27] R.S. Fishman, J.T. Haraldsen, N. Furukawa, and S. Miyahara, Phys. Rev. B **87**, 134416 (2013).
[28] R.S. Fishman, Phys. Rev. B **87**, 224419 (2013).
[29] J.J. Hopfield and D.G. Thomas, Phys. Rev. Lett. **4**, 357 (1960).
[30] D. Szaller, S. Bordács, I. Kézsmárki, Phys. Rev. B **87** 014421 (2013).
[31] I. Kézsmárki, N. Kida, H. Murakawa, S. Bordács, Y. Onose, and Y. Tokura, Phys. Rev. Lett. **106**, 057403 (2011).
[32] S. Bordács, I. Kézsmárki, D. Szaller, L. Demkó, N. Kida, H. Murakawa, Y. Onose, R. Shimano, T. Rõõm, U. Nagel, S. Miyahara, N. Furukawa, and Y. Tokura, Nat. Phys. **8**, 734 (2012).
[33] S. Miyahara and N. Furukawa, J. Phys. Soc. Japan **80**, 073708 (2011).
[34] I. Kézsmárki, D. Szaller, S. Bordács, B. Kocsis, Y. Tokunaga, Y. Takuchi, H. Murukawa, Y. Tokura, H. Engelkamp, T. Rõõm, and U. Nagel, Nat. Comm. **5**, 3023 (2014).
[35] Y. Takahashi, Y. Yamasaki, and Y. Tokura, Phys. Rev. Lett. **111**, 037204 (2013).
[36] Y. Takahashi, R. Shimano, Y. Kaneko, H. Murakawa, and

Y. Tokura, Nat. Phys. **8**, 121 (2012).
[37] I. Kézsmárki, U. Nagel, S. Bordács, R.S. Fishman, J.H. Lee, H.T. Yi, S.-W. Cheong, and T. Rõõm (*unpublished*).
[38] H. Katsura, N. Nagaosa, and A.V. Balatsky, Phys. Rev. Lett. **95**, 057205 (2005).
[39] R.S. Fishman, Phys. Rev. B **88**, 104419 (2013).
[40] J.-H. Lee and R.S. Fishman, (*unpublished*).
[41] R. deSousa and J.E. Moore, Phys. Rev. B **77**, 012406 (2008).
[42] When $\mathbf{m} = [0, 0, 1]$, a field-independent feature was reported in Ref.[19] at 16.3 cm^{-1}. Because it did not fit into our mode scheme, this feature was difficult to understand. A re-examination of the THz data reveals that the total area of the nearly-degenerate $\Psi_0/\Phi_1^{(1)}$ modes at zero field was erroneously reported too high (6.9 ± 1.0 cm^{-2}) by Ref.[19]. The correct value is 3.5 ± 0.3 cm^{-2} and there is no magnetic field independent mode at 16.3 cm^{-1}. Hence, it does not appear in Fig.4(a).
[43] It is questionable whether Ref.[18] actually observed the nearly-degenerate $\Psi_0/\Phi_1^{(1)}$ modes at zero field: the reported frequency of 18.4 cm^{-1} is substantially higher than the 16.2 cm^{-1} mode seen in Fig.4. In Faraday measurements, Ref.[19] also observed a feature in the absolute spectrum around 18 cm^{-1} at zero field. Since this feature does not appear in a magnetic field, it may be an interference fringe rather than an actual mode of the cycloid.
[44] C. Jia, S. Onoda, N. Nagaosa, and J.H. Han, Phys. Rev. B **76**, 144424 (2007)
[45] T.A. Kaplan and S.D. Mahanti, Phys. Rev. B **83**, 174432 (2011).
[46] M. Mostovoy, Phys. Rev. Lett. **96**, 067601 (2006).
[47] I.A. Sergienko and E. Dagotto, Phys. Rev. B **73**, 094434 (2006).
[48] R. deSousa, M. Allen, and M. Cazayous, Phys. Rev. Lett. **110**, 267202 (2013).
[49] A polar vector does not change sign under spatial inversion but an axial vector does. Under spatial inversion,

$$W_{1x} = \frac{1}{N} \sum_{\mathbf{R}_i, \mathbf{R}_j = \mathbf{R}_i + a\mathbf{x}} \mathbf{S}_i \cdot \mathbf{S}_j$$
$$\rightarrow \frac{1}{N} \sum_{\mathbf{R}_i, \mathbf{R}_j = \mathbf{R}_i - a\mathbf{x}} \mathbf{S}_i \cdot \mathbf{S}_j = W_{1x}.$$

Since similar relations hold for W_{1y} and W_{1z}, $\mathbf{W}_1$ is a polar vector. On the other hand,

$$W_{2x} = \frac{1}{N} \sum_{\mathbf{R}_i, \mathbf{R}_j = \mathbf{R}_i + a\mathbf{x}} (-1)^{n_i} \mathbf{S}_i \cdot \mathbf{S}_j$$
$$\rightarrow \frac{1}{N} \sum_{\mathbf{R}_i, \mathbf{R}_j = \mathbf{R}_i - a\mathbf{x}} (-1)^{n_i} \mathbf{S}_i \cdot \mathbf{S}_j = -W_{2x}$$

because $n_i = n_j + 1$ for $\mathbf{R}_i$ and $\mathbf{R}_j = \mathbf{R}_i - a\mathbf{x}$. Therefore, $\mathbf{W}_2$ is an axial vector but $\mathbf{z}' \times \mathbf{W}_2$ is a polar vector.
[50] S. Miyahara and N. Furukawa, Phys. Rev. B **89**, 195145 (2014).
[51] Assuming the simple coplanar cycloid of Eqs.(6-8), symmetry dictates (I. Kézsmárki, *unpublished*) that $\Delta\alpha(\omega) = 0$ when $\mathbf{m} \perp \mathbf{x}'_m$ and either $\mathbf{e}$ or $\mathbf{h}$ lies along $\mathbf{x}'_m$ for domain m. Those two conditions are met for domain 1 with $\mathbf{x}'_1 = [1, -1, 0]$ when $\mathbf{m} = [\eta, \eta, \kappa]$, $\mathbf{k} = [0, 0, \pm 1]$, and either $\mathbf{e} = [1, 1, 0]$ or $[1, -1, 0]$. This argument implies that NDD should vanish for static magnetic fields along $[0, 0, 1]$ and $[1, 1, 0]$ but appear for field along $[1, -1, 0]$, when domains 2 and 3 are stable and degenerate[39]. Although this symmetry argument fails when the cycloid is distorted by a magnetic field, our numerical results suggest that $\Delta\alpha(\omega)$ vanishes when the two conditions above are satisfied.
[52] See, for example, P.R. Bevington, *Data Reduction and Error Analysis for the Physical Sciences* (McGraw Hill, New York, 1969), Section 11.5. The parameters in Table II for fit 2 are very close to those in Ref.[37], which did not include the 2 T data set due to its small NDD. The error bars in Table II are also close to those in Ref.[37], which undertook a more sophisticated analysis based on the covariance.
[53] About 3% of the light intensity has the wrong (perpendicular) polarization. This misalignment is more severe for the Voigt geometries ($\mathbf{m} = [1, -1, 0]$ and [1,1,0]) than for the Faraday geometry ($\mathbf{m} = [0, 0, 1]$).
[54] J.-H. Lee, I. Kézsmárki, and R.S. Fishman, (*unpublished*).
[55] H.J. Xiang, P.S. Wang, M.-H. Whangbo, and X.G. Gong, Phys. Rev. B **88**, 054404 (2013).
[56] X.Z. Lu, X. Wu, and H.J. Xiang, Phys. Rev. B **91**, 100405(R) (2015).
[57] M. Tokunaga, M. Akaki, T. Ito, S. Miyahara, A. Miyake, H. Kuwahara, and N. Furukawa, Nat. Comm. **6**, 5878 (2015).
[58] S. Miyahara and N. Furukawa, J. Phys. Soc. Japan **81**, 023712 (2012).
[59] H.B. Chen and Y.-Q. Li, Applied Physics Letters **102**, 252906 (2013).
[60] C. Weingart, N. Spaldin, and E. Bousquet, Phys. Rev. B **86**, 094413 (2012).
[61] P.E. Blöchl, *Phys. Rev. B* **50**, 17953 (1994).
[62] G. Kresse and D. Joubert, *Phys. Rev. B* **59**, 1758 (1999).